Energy & Environmental Science

REVIEW

View Article Online
View Journal | View Issue

Cite this: *Energy Environ. Sci.*, 2019, **12**, 41

Layered and two dimensional metal oxides for electrochemical energy conversion

Michelle P. Browne, Zdeněk Sofer and Martin Pumera *

The oxygen evolution and reduction reactions are two extremely important reactions in terms of energy applications. Currently, the Oxygen Evolution Reaction (OER) hinders the efficient running of electrolyzer devices which convert water into molecular H_2. This H_2 can subsequently be used in a H_2/O_2 fuel cell for the renewable generation of electricity with only H_2O as a by-product. However, this fuel cell process is not economy feasible due to the sluggish kinetics of the Oxygen Reduction Reaction (ORR) at the device cathode, even with expensive state-of-the-art electrocatalytic materials. As of late, the amount of interest in the OER and ORR, from research laboratories from all over the globe, has risen rapidly in order to find cheap and efficient catalysts to replace the expensive platinum based catalysts currently used in the two aforementioned energy conversion/generation technologies. Layered transition metal oxides, based on the cheap transition metal oxides Mn, Co, Ni and Fe have been reported as viable catalysts for the OER and ORR. Layered structures have an added advantage over non-layered materials as the surface area can be increase by means of exfoliation, with potential for tailoring electrocatalytic activity. It has been shown that the fabrication process and post-synthetic treatments, *e.g.* anion exchange or exfoliation, of these materials can alter the catalytic activity of these materials. Here we summarise various fabrication methods and modifications utilised in literature to tailor the performance of layered transition metal and hydroxide based catalysts for the ORR and OER toward that of the state-of-the-art materials for these technologies.

Received 26th August 2018,
Accepted 4th October 2018

DOI: 10.1039/c8ee02495b

rsc.li/ees

Center for the Advanced Functional Nanorobots, Department of Inorganic Chemistry, University of Chemistry and Technology Prague, Technicka 5, 166 28 Prague 6, Czech Republic. E-mail: martin.pumera@vscht.cz

Michelle P. Browne

Michelle Browne is a ChemJets research fellow in the group of Prof. Martin Pumera at the University of Chemistry and Technology Prague in the Czech Republic. Prior to this, she was a research fellow on an UK Catalysis Hub Project based in Queens University Belfast in the United Kingdom. In 2017, Michelle received her PhD from Trinity College Dublin, Ireland, in electrochemistry and material science under the supervision of Prof. Mike Lyons and Prof. Paula Colavita.

Zdeněk Sofer

Zdeněk Sofer is an Associate Professor at the University of Chemistry and Technology Prague since 2013. He received his PhD also at University of Chemistry and Technology Prague, Czech Republic, in 2008. During his PhD he spent one year in Forschungszentrum Julich (Peter Grünberg Institute, Germany) and also one post-doctoral stay at University Duisburg-Essen, Germany. Research interests of Prof. Sofer concerning on nanomaterials graphene based materials and other 2D materials, its chemical modifications and electrochemistry. He is an associated editor of FlatChem journal. He has published over 310 articles, which received over 6000 citations (h-index of 39).

Broader context

Research into finding economical and sustainable energy alternatives to the world's ever dwindling fossil fuel reserves has increased significantly in the last decade. One renewable energy generation/distribution route called the hydrogen economy concept is receiving significant attention from research groups. The hydrogen economy concept is one idea which utilises H_2 gas as the main energy source for the efficient running of buildings, homes and vehicles. Unfortunately, due too many inefficiencies associated with the energy conversion device (electrolyser), needed to make the H_2, and the fuel cell device, utilised to convert the H_2 into electricity, this idea remains a concept. Many research laboratories all over the world are trying to fabricate cheap and active catalysts to improve the activity while lowering the cost of the materials needed in these two devices. Finding a cheap and active catalyst which rivals that of the state-of-the-art materials for these devices would make the hydrogen economy concept closer to a reality. Layered materials, compared to their bulk counterpart, have shown improved activity as catalysts for electrolyser and fuel cell technologies. Herein, the effect of the fabrication and post-fabrication methods on the catalytic activity used to make these layered materials for electrolysers and fuels are discussed.

Introduction

The world's energy consumption in 2015 was approximately 9384 million tonnes of oil equivalent (Mtoe).[1] Alarmingly, the world energy consumption has increased by 50.33% since the International Energy Agency began to publish the Key World Energy Statistics Document in 1974.[1] Of this energy consumption value, 85.5% was produced by fossil fuels alone, with the rest of the energy being produced from other sources including renewable energies. There are many disadvantages associated with fossil fuel combustion including the release of gaseous exhausts which can act as precursors to smog or acid rain. As well as the production of carbon based emissions which, when combusted, have detrimental effects on our environment by facilitating an increased greenhouse effect.[2] However, the main disadvantage associated with fossil fuels is that the current fossil fuel reserve is predicted to be depleted by the year 2112, with coal being the only fossil fuel available after the year 2042.[3] Subsequently, alternative routes of producing cheap and environmentally clean energy are currently undergoing major research.[4,5]

One alternative route of interest is using fuel cells to generate energy.[6–8] For example, porous membrane hydrogen fuel cells use only H_2 and O_2 gas to generate electricity with H_2O as the sole exhaust product. However, the H_2 used in these fuel cells is typically produced from a fossil fuels source.[9] Currently 95% of the world's hydrogen production is a product of a fossil fuel based route while only 5% of hydrogen is generated by alternative routes including water electrolysis.[10]

Hydrogen has been described as the ultimate clean energy source.[11] Molecular hydrogen not only possesses a higher gravimetric energy density when compared with traditional fossil fuels, but can also be utilised to develop clean energy devices for the generation of electricity for national grids around the world. This concept is basis on the so-called hydrogen economy idea, which consists of the production of molecular hydrogen from renewable resources, its storage for later usage, distribution to local fuel cell sites, and utilisation in a fuel cell in order to generate electricity, Fig. 1.[12–14]

In the last five years electrochemical water splitting has become a technology of continuously increasing interest to the wider scientific community in a bid for the search for renewable fuels to replace the worlds' ever dwindling fossil fuel reserves. Water electrolysis splits water into hydrogen at the cathode and oxygen at the anode, denoted as the Hydrogen Evolution Reaction (HER) and the Oxygen Evolution Reaction (OER), respectively.[15–17] This process usually takes place in either acidic or alkaline media, as ionic species are needed to be present for the reaction to proceed. The overall reaction and the reactions which proceed in both media can be represented as follows:[18]

$$2H_2O + \text{energy} \rightarrow 2H_2 + O_2 \quad (1)$$

In alkaline solutions, the reactions at the anode and cathode are:[19,20]

$$4OH^- \rightarrow O_2 + 2H_2O + 4e^- \quad \text{(Anode)} \quad (2)$$

Martin Pumera

Martin Pumera is currently the Director of the Center for Advanced Functional Nanorobots at the University of Chemistry and Technology, Prague, Czech Republic (since 2017). Before joining UCT, he was a tenured faculty member at Nanyang Technological University, Singapore (since 2010). He received his PhD at Charles University, Czech Republic, in 2001. After two postdoctoral stays (in the United States and Spain), he joined the National Institute for Materials Science, Japan, in 2006 for a tenure-track arrangement and stayed there until Spring 2008, when he accepted a tenured position at NIMS. In 2010, he joined NTU Martin has broad interests in nanomaterials and microsystems, in the specific areas of electrochemistry and synthetic chemistry of 2D nanomaterials, micro and nanomachines, and 3D printing.

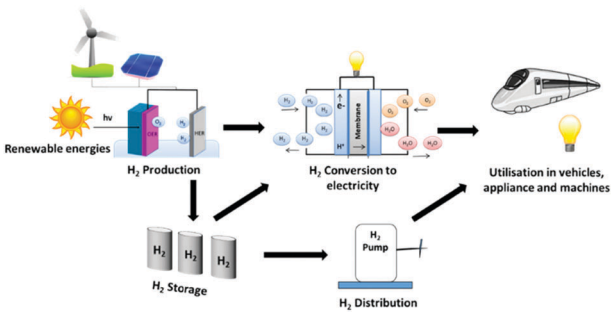

Fig. 1 Schematic of a simple hydrogen economy concept.

$$4H_2O + 4e^- \rightarrow 2H_2 + 4OH^- \quad \text{(Cathode)} \qquad (3)$$

In acidic solutions, the reactions at the anode and cathode are:[21]

$$2H_2O \rightarrow O_2 + 4H^+ + 4e^- \quad \text{(Anode)} \qquad (4)$$

$$4H^+ + 4e^- \rightarrow 2H_2 \quad \text{(Cathode)} \qquad (5)$$

The overall cell potential needed to drive water electrolysis is dependent on the thermodynamic potential of water electrolysis, the overpotentials associated with the reaction on the anode/cathode and the cells ohmic drop.

$$E(i) = E_0 + \eta_a + |\eta_c| + iR \qquad (6)$$

where $E(i)$ is the voltage that should be supplied to the cell for water electrolysis to occur, E_0 is the thermodynamically potential of water electrolysis (1.23 V *vs.* Reversible Hydrogen Electrode (RHE)), η_a and η_c are the overpotentials associated with the anodic and cathodic reactions, respectively, and iR refers to the ohmic drop.[11,22]

The energy required to drive this reaction can be generated from two routes; combining renewable energy technologies, such as wind, hydro or solar stations, with electrolyzer arrays, or incorporating appropriate semi-conductor materials (*e.g.* Fe_3O_4 or TiO_2) with an active electrocatalyst as the working electrode in the electrolyzer and directly shining sunlight onto the electrode of interest, Fig. 2(a). The overall process of water splitting is hindered by the reaction on the anode, the OER, due to the large thermodynamic overpotential associated with this half reaction when compared to the cathodic reaction, the HER.[23] Thus, for the overall water electrolysis process to become more efficient, significant advances must be continuously made in the field which mainly focus on discovering cheap, active catalysts to replace the current commercial standards for the OER in an electrolyser device.[23] Additionally, research into the HER must still be on-going in parallel with the OER as any decrease in the overpotential for either reaction will result in a significant lowering of the cost of the process that will bring us one step closer to a hydrogen economy.[24–27]

Currently, the most efficient catalysts utilised commercially for the OER are based on the expensive and rare elements from the Platinum Group Metals (PGMs). In both acidic and basic media, RuO_2 and IrO_2 are considered the state-of-the-art materials for the OER reaction.[28–31] However, the high cost of these materials compared to other metals combined with their lack of abundance renders their widespread use in commercial devices uneconomical.[32,33] One should also note, another alternative way to potentially increase the efficiency of the HER is to couple this reaction with a thermodynamically more favourable reaction such as the Urea Oxidation Reaction (UOR).[34–36] The UOR has a thermodynamic overpotential of 0.37 V which is approximately 0.9 V lower than the OER.[34] However the UOR also suffers from high overpotential values (*ca.* 1 V) which places most of the UOR catalysts in literature near to the same activity of the OER catalysts on the RHE scale. For example, Yu *et al.*, recently reported that a cheap TMO based catalyst exhibited a potential of 1.38 V *vs.* RHE at 10 mA cm^{-2} for the UOR.[34] Alternatively, Zhang and co-workers recently reported that a low cost FeCoW evolved O_2 at a current density of 10 mA cm^{-2} utilising a potential of 1.42 V *vs.* RHE.[37] The catalysts reported in the two aforementioned studies, for the UOR and OER, are among the best catalysts in literature for their respective reactions. Hence, research into the generation of H_2 by water electrolysis and other routes using a sacrificial reagent, *e.g.* urea, glucose *etc.*, needs to be undertaken concurrently by the scientific community.[34,38]

Another extremely important reaction that suffers from inefficiency involved in the hydrogen economy idea is the Oxygen Reduction Reaction (ORR) which is a critical half-cell reaction in a H_2/O_2 fuel cell.[39,40] This technology promises a clean energy conversion device utilised in-conjunction with an electrolyser to deliver electricity to the masses, Fig. 2(b). At a basic level, a fuel cell consists of an anode plate, a cathode plate and a proton selective membrane *i.e.* Nafion. In a H_2/O_2 fuel cell, H_2 is delivered to the anode where the Hydrogen Oxidation Reaction (HOR) takes place, while the ORR takes place at the cathode plate. The overall reaction that takes place in a fuel cell and the reactions which proceed in both acidic and basic media for the HOR and ORR can be represented as follows:[41–43]

$$2H_2 + O_2 \rightarrow 2H_2O + \text{energy} \qquad (7)$$

In alkaline solutions, the reactions at the anode and cathode are:

$$2H_2 + 4OH^- \rightarrow 4H_2O + 4e^- \quad \text{(Anode)} \qquad (8)$$

$$O_2 + 2H_2O + 4e^- \rightarrow 4OH^- \quad \text{(Cathode)} \qquad (9)$$

In acidic solutions, the reactions at the anode and cathode are:

$$H_2 \rightarrow 2H^+ + 2e^- \quad \text{(Anode)} \qquad (10)$$

$$O_2 + 4H^+ + 4e^- \rightarrow 2H_2O \quad \text{(Cathode)} \qquad (11)$$

Unfortunately, similarly to the OER, the ORR suffers from sluggish kinetics due to multiple electron transfer processes occurring at the electrode interface. Additionally, the use of expensive platinum catalysts deems this process economically unfeasible. The state-of-the-art Pt catalysts for the ORR are also highly susceptible to impurities which makes the Pt materials less stable over time and decreases the material's ability to catalyse the ORR.[44] A viable route around the problems encountered during the ORR and OER is to find low cost, stable and highly

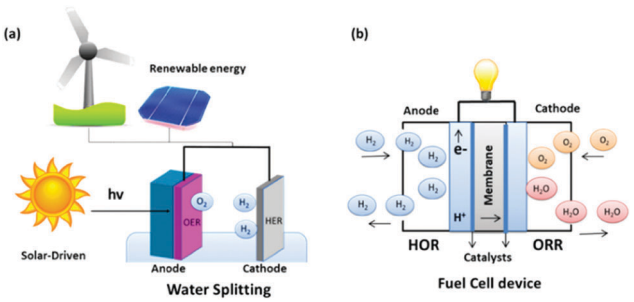

Fig. 2 Schematic of (a) water splitting and (b) fuel cell device.

active materials for these reactions which would, in turn, decrease the overall expenditure associated with using the electrolyser/fuel cell energy production path.[45] For these reasons, a dramatic recent increase in research has taken place into other Transition Metal Oxides (TMOs) from the first row of the d-block of the periodic table.[46–49] This research trend is focused on finding materials which offer cheap and active alternatives to the critical PGMs for these two aforementioned O_2 reactions.[33,50–60]

Layered transition metal oxides and hydroxides

TMOs are composed of a transition metal from the d-block of the periodic table with oxygen. TMOs have many advantages including the ability to change their bonding structure, and hence their oxidation states, as a function of applied annealing temperature during material fabrication or applied electrochemical potential *in situ*; which allows for the evaluation of the OER and ORR of the same material.[61] Of particular interest to various energy applications, such as OER and ORR, are layered TMOs. Layered TMOs consist of stacked quasi-2D sheets weakly held together by van deer's Walls interactions with strong in-plane covalent bonds. These structural properties allow for these materials to be easily exfoliated into their individual quasi-2D structures by various techniques.[62–65]

Additionally, 2D or few-layer TMO based materials can also be achieved by manipulating/treating Layered Double Hydroxide (LDH). These materials consist of brucite-like layers, consisting of MO_6 octahedral sites, which are positively charged. The overall net charge of these structures are achieved by anions or solvation molecules intercalated in between the layers.[66,67] The most common LDH materials consist of two metal centers for the MO_6 sites and the chemical formula for these materials are:[68]

$$[M_{1-x}{}^{2+}M_{3+x}(OH)_2][A^{n-}]_{x/n}\cdot zH_2O \quad (12)$$

where M^{2+} are divalent ions, *e.g.* Mg^{2+} or Ni^{2+}, and M^{3+} are trivalent ions, *e.g.* Fe^{3+} or Mn^{3+}, and the A^{n-} renotes the charge neutralising anion, *e.g.* $CO_3{}^{2-}$. Additionally, there also exists are sub-class of LDH that are only made up of one metal center and no charge neutralising anions or solvation ions are present as there is no positive charge associated with the brucite layers. These materials are called hydroxides and have the chemical formula related to these materials is simplified to:

$$[M(OH)_2] \quad (13)$$

In literature both, anion exchange and exfoliation techniques have been utilised on LDH to optimise these materials for electrochemical oxygen reactions. The anion exchange process replaces the natural charge balancing ions between the basal planes with larger ions which increases the interlayer spacings between the basal planes, making these 2D/few layer materials an attractive option for electrochemical applications.[63,69]

Regardless of the class of the layered material, the 2D form of these layered TMOs often possess enhanced electrochemical properties compared to their bulk counterpart.[70] The fabrication or synthesis of these layered catalysts spans a multitude of various routes including solvothermal,[71] hydrothermal,[72] microwave-assisted,[73] thermal decomposition,[74] low temperature synthesis,[75] and precipitation methods.[70] Then, other treatment processes including anion exchange and exfoliating processes, including chemical, mechanical and physical, are undertaken on these layered materials to enhance its electronic and chemical properties.[76] A table of common layered TMO based materials, the synthetic route to produce the layered materials along with their exfoliated counterpart or anion exchange procedure, if applicable, found in literature that are utilised as catalysts in electrochemical energy applications are illustrated in Table 1.

Structures, fabrication routes and basic properties of common layered transition metal oxide catalysts utilised in O_2 electrocatalysis

Binary layered oxides of transition metals

From the simple binary transition metal oxides, only a minority adopt a layered structure *e.g.* vanadium pentoxide, molybdenum trioxide and tungsten trioxide. The structure of layered transition metal oxides like vanadium(v) oxide, molybdenum(vi) oxide and hydrated tungsten(vi) oxide are shown on Fig. 3. These oxides are relatively volatile and large crystals can be prepared by a sublimation process under partially control oxygen pressure to avoid reduction of the materials.[81,82] Exfoliation of these materials can be performed by mechanical methods; such as share force milling in appropriate solvents.[83] In particularly, MoO_3, and to a lesser extent the other binary transition metal layered oxides mentioned, are known to be catalytic for heterogeneous chemical reactions such as the ORR and OER.[84] In literature, the catalytic activity of these materials can be related to the oxygen vacancies or possible formation of sub-oxides since these oxides tend to form various non-stoichiometric oxidic phases. These oxidic materials are typically synthesised on highly conductive material with large surface areas like graphene based materials. It has been shown, that the interaction of carbon based materials with these nanostructured oxides has resulted in synergic effects on the resulting catalytic properties.[85]

The other group of binary layered oxides with a layered structure are based on transition metal oxide which were synthesised using suitable planar templates, for example TiO_2.[86,87] However, these materials have amorphous or non-layered crystallographic structure and exhibit highly anisotropic shape (platelet shape with single or few layers atoms thickness). The synthesis is typically based on self-assembling methods or by topochemical reactions (*e.g.* conversion of layered TiS_2 into TiO_2 sheets).[86,87] The flexibility and variability of these methods allows for the synthesis of the most basic binary oxides.

Mixed transition metal layered oxides

The mixed transition metal is formed with an alkali metal adopting layered structure. The most typical examples are Li_xCoO_2 or

Table 1 Fabrication route overview of common layered and 2D TMOs in literature

Layered TMO	Fabrication routes	Notes	Ref.
MnO_2	Room temperature wet chemistry (precipitation) and liquid phase exfoliation	MnO_2 nanosheets: $Mn(NO_3)_2{\cdot}H_2O$ + DI-water + PEG–PPG–PEG mixed together and heated. A $KMnO_4$ solution added dropwise until brown precipitate formed. Exfoliation: in IPA using sonic bath and centrifugation.	70
MnO_2	Thermal decomposition and sulfurisation process	Thermal decomposition: graphene oxide + $KMnO_4$ mixed in water at 80 °C for 24 hours. Then filtered, washed and dried. Sulfurisation process: MnO_2 mixed with sulphur powder in a alumina crucible and calcined in a tube furnace for 12 hours under N_2 flow. The temp was then raised to 250 °C and heated for an hour under N_2 to evaporate the excess S.	74
MnO_2	Thermal decomposition	Thermal decomposition: $KMnO_4$ heated at 500 °C for 5 hours. Then washed with DI water and dried at 80 °C overnight.	77
$Ni(OH)_2$	Liquid phase exfoliation of commercial powder	Exfoliation: carried out in sodium cholate in both water and *N*-methyl-pyrrolidone in a metal beaker using an ultrasonic tip. Then centrifugation to select nanosheet size.	78
$Ni(OH)_2$	Hydrothermal synthesis	Hydrothermal: nickel nitrate, Oleylamine and water were stirred for 30 min and transferred to an autoclave. The reaction vessel was annealed at 180 °C for 15 hours.	54
$Co(OH)_2$	Liquid phase exfoliation of commercial powder	Exfoliation: carried out in sodium cholate/isopropyl alcohol in a metal beaker using an ultrasonic tip for 4 h. Then centrifugation to select nanosheet size.	79
Co–Co LDH and Ni–Co LDH	Topochemical synthesis and anion exchange.	Topochemical synthesis: Ni and/or Co chloride salt + hexamethylenetetramine refluxed for 5 hours at 90 °C to produce the hydroxide. To fabricate the LDH*, the hydroxide + Br_2 + acetonitrile was magnetically stirred for 1 and 5 days for the Co–Co LDH and the Ni–Co LDH, respectively. Anion exchange: ethanol assisted anion exchange using sodium nitrate (NO_3^- ions).	67
Ni–Fe LDH	Hydrothermal synthesis and anion exchange.	Hydrothermal synthesis: nickel and iron nitrate salts mixed with urea + triethanolamine + water and transferred to a stainless steel Teflon cup and heated for 2 days at 150 °C. Anion exchange: ethanol assisted anion exchange using sodium chloride (Cl^- ions).	67
Ni–Fe LDH	Co-Precipitation and chemical exfoliation	Co-Precipitation: a $NaOH/Na_2CO_3$ solution was added dropwise to Ni and Fe nitrate salts. The suspension was stirred for 10 min and then heated to 65 °C for 24 hours. Exfoliation: Ni/Fe oxide dispersed in formamide and stirred under N_2 atmosphere for 2 days. The solution was then centrifuged to remove un-exfoliated material.	80

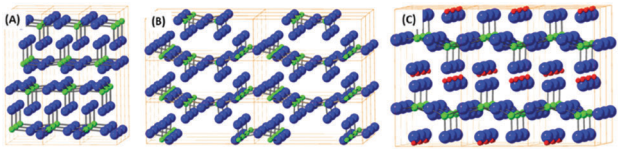

Fig. 3 The structural model of molybdenum(VI) oxide (A), vanadium(V) oxide (B) and hydrated tungsten(VI) oxide (C). Yellow lines show elemental cells, blue balls are oxygen atoms, green balls are metals atoms and red ball are hydrogen atoms.

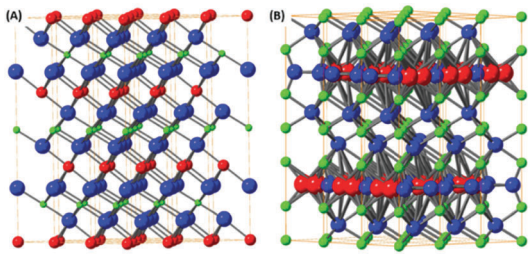

Fig. 4 The structural models of layered oxides containing alkali metal and transition metal. The structure of $LiCoO_2$ (A) and (B) mineral birnessite ($K_{0.48}Mn_{1.97}O_{5.18}$) based on layers of alkali metals and oxygen octahedrally coordinated transition metal layer.

K_xMnO_2 where the structure is based on hexagonally coordinated metal ions with oxygen and alkali metal atom layers. Due to the possibilities in the variation of alkali metal content these materials are highly popular for battery applications.[88] The Li_xCoO_2 structure is shown on Fig. 4(A). However, these materials don't adopt true van der Waals layered structure therefore they can be exfoliated by chemical methods based on substitution/removal of alkali ions intercalated between the metal-oxide layers.[89] The family of this type of layered oxides is very rich and from the ternary based systems K_xMnO_2, also called δ-MnO_2 oxide or birnessite according its natural counterpart, is well known, Fig. 4(B). The other layered oxides in this family of materials can be based on iron, chromium, titanium and other transition metals.[90] Transition metals form also several complex layered oxidic phases including titanates, tantalates, niobates, tungstates and its various mixed counterparts. Similarly, to birnessite type oxides, their exfoliation is based on the removal or substitution of alkali metals within layered structure. Their substitution with bulky ions, such as tetrabutylammonium ions, treatment with acids (hydrated protonic form) and subsequent reaction with tetrabutylammonium hydroxide significantly increase interlayer spacing and allows for their mechanical exfoliation to take place. These complex oxides exhibit several interesting physical properties including thermoelectric effects, ferroelectric and multiferroic properties, but to date their exploration as electrocatalysis for the OER and ORR has been very limited.

Layered hydroxides, oxo-hydroxides and double layered hydroxides

The layered hydroxides are dominantly based on the brucite structural type, where the metal ion is hexagonally coordinated with six hydroxyls. Most of the M^{2+} transition metal sites adopt a hydroxide structure *e.g.* $Fe(OH)_2$, $Co(OH)_2$ and $Cu(OH)_2$. The typical crystal structure of brucite type materials is shown in Fig. 5(C). Several of these hydroxides have limited stability issues with regard to pH, as well as their oxidation state. All of these brucite type oxides tend to dissolve at low pH and some at high pH values due to the formation of hydroxocomplex species *e.g.* $[Zn(OH)_4]^{2-}$. This problem can raise issues when investigating these materials for the OER and ORR as low/high pH solutions are utilised during experimental studies. The oxidation sensitivity is especially pronounced for $Fe(OH)_2$ even when pyrophyric in its powdered dry state. The fabrication procedure is typically based on topochemical reactions which yield layered oxo-hydroxide materials.[91,92]

Based on the layered hydroxide structure, there also exist a broad group of layered oxide-hydroxide of general formula MO(OH) which are generally formed by topochemical oxidation of layered hydroxides (*e.g.* lepidocrocite γ-FeO(OH)). The structure is shown on Fig. 5(A). The oxo-hydroxides are significantly more stable in comparison with metal hydroxides and can withstand relatively broad pH range, especially in alkaline environment.

An important group based on the brucite structure for the OER and ORR are the layered double hydroxides (LDH). The LDH structure consists of M^{2+} ions substituted with M^{3+} ions and in-between layers charge compensation anions, *e.g.* hydroxides, carbonates *etc.*, are present. The structure of these materials are extremely varied; multiple possibilities for the anion and cation sites exist as well as the anion introduction into the interlayer space between hydroxide structures. The LDH structure can be observed in Fig. 5(B). The presence of multivalence ions results in a positive charge for the hydroxide layers compensated by lightly bonded anions. The general formula of LDH can be written as $M_{1-x}^{2+}M_x^{3+}(OH)_2 \cdot A_{x/n}^{n-} \cdot mH_2O$ where $M^{2+} = Mg^{2+}$, Fe^{2+}, Co^{2+}, Ni^{2+}, Zn^{2+} and others and $M^{3+} = Al^{3+}$, Fe^{3+}, Cr^{3+} and others. The synthesis is typically based on

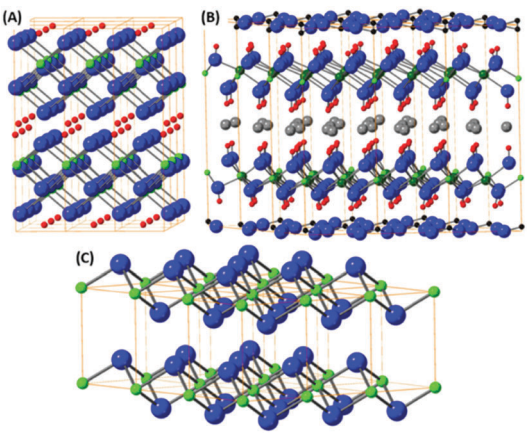

Fig. 5 (A) The structures derived from layered oxo-hydroxide MO(OH); (B) the structure of double layer hydroxide (hydrotalcite with composition $Al_2Mg_4(OH)_{12}(CO_3)\cdot 3H_2O$). (C) The structural model of layered hydroxide with brucite structural type of general formula $M(OH)_2$; metal atoms are green, oxygen atoms blue, hydrogen atoms red and carbon atom black. Grey atoms in LDH.

reaction of metallic ions at elevated pH (formed *e.g.* by thermal decomposition of urea under hydrothermal conditions). The presence of organic long chain anions like dodecylsulfate or lactate can form LDH with controlled and extremely high interlayer spacing. Such LDH with large interlayer spacing can be easily exfoliated by mechanical exfoliation like share force milling or ultra-sonication. Since the LDH can slowly dissolve at high pH (*e.g.* containing Al^{3+}) or at lower pH, neutral solvents like water, alcohols or hydrocarbons are used. The presence of catalytically active transition metals, *e.g.* Mn, Fe, Ni and Co, in the LDH structure have made these materials an attractive option to study as OER and ORR catalysts throughout literature.

In recent years the amount of literature reported on the OER and ORR using layered TMOs has steadily increased however the impact may be over shadowed by the more popular Transition Metal Dichalcogenides (TMDs) for the HER. This review highlights and discusses recent research in the area of OER and ORR which utilise layered and 2D TMO materials as catalysts. With particular emphasis on how the fabrication route and additives/enhancement aids *e.g.* carbon nanotube as support for increased conductivity, can affect the performance of these important O_2 reactions that are central to the implementation of a future hydrogen economy.

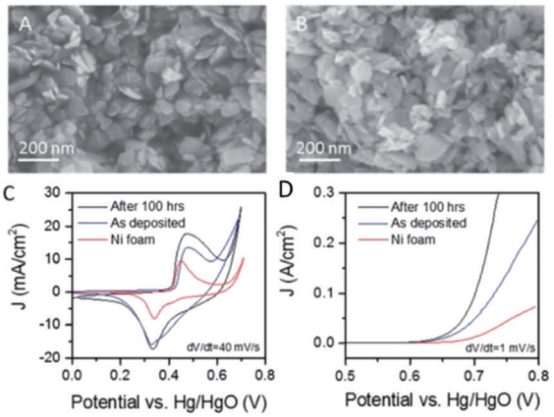

Fig. 6 Liquid exfoliated $Ni(OH)_2$ nanosheets. (A and B) SEM images of an as-prepared $Ni(OH)_2$ film and (B) a film after activation by 100 h polarisation with current density of 10 mA cm^{-2}. (C) Cyclic voltammograms measured for supercapacitor electrodes fabricated from $Ni(OH)_2$ films on Ni foam current collectors before and after activation. A CV curve measured for the bare Ni foam is shown for comparison. (D) Polarisation curves for OER from $Ni(OH)_2$ electrodes fabricated from $Ni(OH)_2$ films on Ni foam current collectors before and after activation with the equivalent curve for the bare Ni foam shown for comparison. (Reproduced with permission (ref. 78) Copyright Royal Society of Chemistry (2016).)

Oxygen evolution reaction (OER)

It is widely accepted that variations in the synthetic route and/or electrode fabrication technique can greatly affect the performance and stability of catalysts for electrochemical energy processes.[93,94] Therefore, and more specifically, investigating appropriate pathways to produce and fixate layered TMO catalysts on suitable current collectors for the optimisation of the OER is a major area of research that is currently on-going.[95] Moreover, further processing techniques and/or conductive aids have been reported to further enhance 'bare' layered TMOs for the OER.[76] Multiple studies on layered TMO catalysts will be compared and discussed herein to evaluate and understand the optimum fabrication parameters in respect to their OER performance.

Cheap layered TMOs, *e.g.* Ni(OH), $Co(OH)_2$, MnO_2 and NiFe based materials, from the first row of the transition metals (d-block) periodic table have received an increasing amount of interest as of late as catalysts for the OER. Liquid phase exfoliation (LPE) of $Ni(OH)_2$ and $Co(OH)_2$ layered materials has been reported to increase the activity of these materials for the OER compared to their layered stucture.[76,78,79] For example, $Ni(OH)_2$ exfoliated by LPE in a iso-propyl alcohol (IPA) dispersion was deposited onto Ni foam by a spraying technique and the OER performance was analysed in 1 M NaOH, Fig. 6(A).[78] Before OER the exfoliated $Ni(OH)_2$ was confirmed by X-ray Photoelectron Spectroscopy (XPS) measurements which revealed no change in the oxidation state of the Ni atoms. However, a broad peak in the O1s core level region was noted for the exfoliated nano-sheets when compared to the pre-treated $Ni(OH)_2$. This broadening was attributed to the utilization of sodium cholate surfactant during the exfoliation process. The OER activity of exfoliated $Ni(OH)_2$ on Ni foam out-performed the bare Ni foam by a factor of 2.5 with respect to current density, Fig. 6(C and D).[78] The authors further enhanced the exfoliated $Ni(OH)_2$/Ni foam electrode by electrochemically polarising the electrode at a current density of 10 mA cm^{-2} for a period of 100 hours; an SEM image of polarised electrode can be observed in Fig. 6(B). The authors suggested, in accordance with previous reports, that the increased performance of the polarised $Ni(OH)_2$ electrode was a result of the conversion of the $Ni(OH)_2$ phase to a more active NiOOH phase before the OER.[96–98] However, since the OER experiments were conducted in NaOH with Fe impurities, it should be noted that this increase in the OER performance of the pre-polarised $Ni(OH)_2$/Ni foam electrode may not be due to a more active NiOOH phase but the substitution of Ni ions by Fe impurity ions from the NaOH electrolyte solution in the $Ni(OH)_2$ lattice. It has been extensively shown that $Ni(OH)_2$ in KOH or NaOH electrolyte with Fe impurities performances as a better OER catalysts than in the same electrolyte with no Fe impurities.[99,100] This substitution was first observed electrochemically by Corrigan *et al.* in the 1980s and more recently numerous groups using materials characterisation techniques *i.e.* XPS and Raman spectroscopy.[99–102]

The same exfoliation process conducted on the layered $Ni(OH)_2$ was applied also to $Co(OH)_2$ which produced nanosheets with the dimensions of 88 nm in length and 94 mm width, Fig. 7(A–E).[76,79] After exfoliation, extensive material characterisation was carried out on the $Co(OH)_2$ to reveal that, unlike the exfoliated $Ni(OH)_2$, XPS showed a slight change in the chemical environment for the $Co(OH)_2$ exfoliated materials, Fig. 7(G and H). However, similarly to the $Ni(OH)_2$, a broad peak in the O1s region is observed which, again, may be due

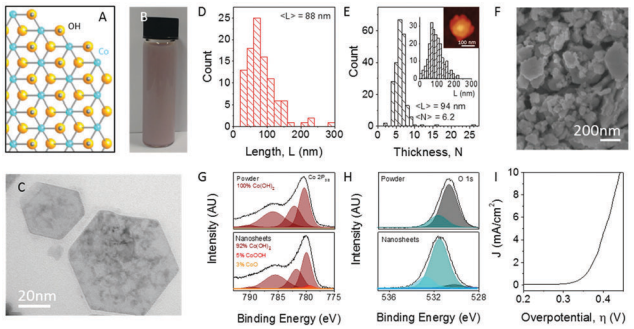

Fig. 7 Exfoliation of $Co(OH)_2$ into nanosheets. (A) Structure of cobalt hydroxide, $Co(OH)_2$. Blue, Co; yellow, O; silver, H. (B) Photograph of typical $Co(OH)_2$ dispersion in surfactant solution (concentration of $Co(OH)_2$ was 7 mg mL^{-1}). (C) Representative low-resolution TEM image of exfoliated $Co(OH)_2$ nanosheets. (D) Nanosheet length distribution as measured by TEM. (E) Nanosheet thickness (layer number) distributions as measured by AFM with length distribution and sample image shown in the inset. (F) SEM image of a vacuum filtered film of $Co(OH)_2$ nanosheets. (G) Co $2p_{3/2}$ XPS spectra of $Co(OH)_2$ pretreated bulk powder (top) and a film of re-aggregated nanosheets (bottom). (H) O 1s core-level spectra of pretreated powder (top) and film of re-aggregated nanosheets (bottom). (I) Polarization curve for an electrode consisting of vacuum filtered $Co(OH)_2$ nanosheets on a glassy carbon electrode (1 M NaOH, scan rate 1 mV s^{-1}). (Reproduced with permission (ref. 76) Copyright Wiley and Sons (2018).)

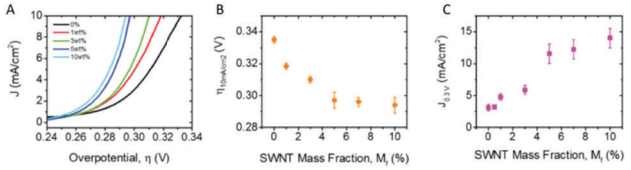

Fig. 8 $Co(OH)_2$–SWNT composite OER catalysts. (A) Linear sweep voltammograms for composite electrodes with a fixed $Co(OH)_2$ loading of 0.9 mg cm^{-2} for a range of nanotube contents. (B) Overpotential required to produce 10 mA cm^{-2} and (C) current density at overpotential of 0.3 V, both plotted as a function of SWNT volume fraction. All figures pertain to s-$Co(OH)_2$ using 1 M NaOH as an electrolyte where applicable. (Reproduced with permission (ref. 76) Copyright Wiley and Sons (2018).)

to the sodium cholate used during the liquid phase exfoliation process.[76,78]

This exfoliated $Co(OH)_2$ was vacuum filtrated onto a GC disk electrode, Fig. 7(F) and measured for its OER performance. As noted by the authors the OER performance of the exfoliated $Co(OH)_2$ was poor. In order to enhance the OER activity of this material, carbon nanotubes (CNTs) in various weight percentages (1–10%) were added to the exfoliated $Co(OH)_2$ dispersion and, again, vacuum filtrated onto GC electrodes, Fig. 8(A). As observed in Fig. 8(B and C), the overpotential at 10 mA cm^{-2} decreases while the current density increase, respectively, with additional CNT weight content to 5% and then levels off. This study indicates there is a maximum amount of CNT content needed to be added to the $Co(OH)_2$ before no more enhancing effects are observed. Unfortunately, according to other reports, CNTs, and to a larger extent multi-walled CNT, can also catalyse the OER, therefore it is not clear if the CNT simply improves the conductivity of the $Co(OH)_2$ network, or whether the CNTs themselves participate in catalysis of the OER.[103]

In a subsequent report by the same group, the exfoliated $Co(OH)_2$ was deposited onto two different types of high area supports; glassy carbon (GC) foam and nickel (Ni) foam.[79] The results reveal the exfoliated $Co(OH)_2$ on the Ni foam was a superior electrode when compared to the same material on the GC foam in terms of absolute OER overpotetnial *i.e.* the overpotential at 10 mA cm^{-2}. This value was 280 and 380 mV for the $Co(OH)_2$ on the Ni and GC foams, respectively, in 1 M NaOH. However, when comparing the activity of the $Co(OH)_2$ catalysts/substrate combination to the bare support in relative terms the $Co(OH)_2$ on the GC support was the more appropriate relationship. The $Co(OH)_2$ on the GC had an improved OER performance by 57% compared to the bare GC, while the $Co(OH)_2$/Ni achieved a 30% increase over the bare Ni support.[79] Interestingly, the $Co(OH)_2$ on the Ni foam behaved as a better OER electrocatalyst when compared to the exfoliated $Ni(OH)_2$ on the same Ni foam support previously discussed in this review by the same group.[78] However, regardless of the actual OER performance values, it is clear that the nature of the support plays a role in the activity of layered TMO material.

In nature, Photosystem II is a molecular complex that is utilised to produce molecular O_2 in plants and algae. This complex is based around a Mn and Ca center. For this reason, bulk Mn-based TMO materials (MnO, Mn_2O_3, Mn_3O_4 and MnO_2) have been extensively studied in literature.[57,61,105–107] However, the OER overpotentials reported for these materials have not yet reached that of the state of the art.[15,16] Recently, few layer/2D δ-MnO_2, also known as birnessite, has emerged as a potential candidate for water splitting. Birnessite occurs naturally and is composed of 2D layers consisting of O ions octahedrally coordinated to a central Mn ion with both Mn^{3+} and Mn^{4+} present. The overall net charge is negative, however charge neutrality is usually governed by the positive charged alkali metal ions (*e.g.* K^+, Na^+) between the 2D layers. The promise of this layered/2D-layer spans multiple reasons including (1) optimum OER active sites for Mn have been postulated to lie between Mn^{3+} and Mn^{4+} and (2) there has been an indication of increased conductivity and electronic properties for few layer/2D birnessite compared to bulk MnO_2.[57,104,108,109]

2D δ-MnO_2 on Ni foam produced by an *in situ* hydrothermal synthesis using $KMnO_4$ and H_2O was investigated for its OER characteristics in 0.1 M KOH, Fig. 9.[104] The OER measurements of the 2D δ-MnO_2 and bulk MnO_2 on Ni foam (not in figure) showed that the 2D δ-MnO_2 was a much superior catalyst; the overpotential at 10 mA cm^{-2} for the 2D MnO_2 was 0.32 V for the exfoliated material while the bulk MnO_2 did not reach this current density at all to allow for the authors to report an overpotential. Interestingly, the 2D δ-MnO_2 material even proved to be better than the OER state of the art OER catalysts, IrO_2, in regards to the overpotetnial at 10 mA cm^{-2} and Tafel slope values, see Fig. 9(A) and (B). The enhanced performance of the 2D δ-MnO_2 was rationalised to be due to the larger electrochemical surface area determined for the 2D material over the bulk; 19.58 and 0.80 mF cm^{-2} respectively, which could be rationalised due to the larger surface area of the 2D nanosheets. Another reason for the increase in the OER activity

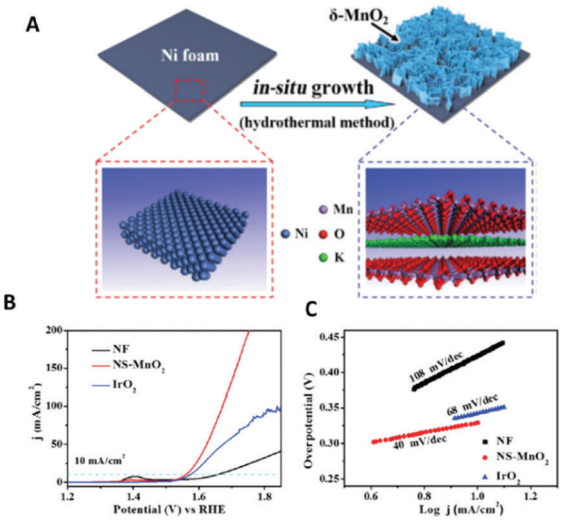

Fig. 9 Schematic showing the *in situ* growth of ultrathin δ-MnO_2 nanosheets on an Ni foam (NS-MnO_2). (A) Linear sweep voltammetry (LSV) curves for OER at a scan rate of 5 mV s^{-1}. (B) Tafel plots for OER. (C) LSV curves for HER at 5 mV s^{-1}. (Reproduced with permission (ref. 104) Copyright Wiley and Sons (2017).)

could be due to the lower oxidation state (Mn^{3+}), revealed by the XANES measurement, that is only observed in the 2D structure of MnO_2 and gives rise to a half-metallic state not observed in bulk MnO_2.

Increasing the interlayer spacing of layered MnO_2 utilising transition metal ions *e.g.* Ni^{2+}, can also affect its OER catalytic abilities.[110] As demonstrated previously the OER activity of this layered material can be tuned by intercalating various amount of Ni^{2+} ions (6.1, 6.5 and 7.7%) into the spacings between the 2D layers by a wet chemical ion exchange reaction during synthesis. This resulted in a decrease in the interlayer spacing with increasing Ni^{2+} %; the interlayer spacings for the 6.1, 6.5 and 7.7% Ni intercalated layered MnO_2 was 7.17, 7.06 and 7.04 Å, respectively. The interlayer spacing for birnessite is typically 7.27 Å.[110]

The OER activity for the layered and intercalated Ni^{2+} MnO_2 was determined in 1 M KOH, see Fig. 10. A noticeable increase in performance for the Ni^{2+} layered MnO_2 over the bare material can be observed. The data shows that with decreasing interlayer spacing, the OER results become more cathodic with the 7.7%

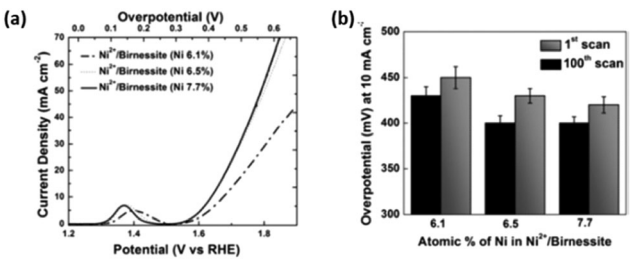

Fig. 10 (a) Polarization curves for Ni^{2+}/birnessite with varying amounts of Ni. (b) Comparison of overpotentials to reach 10 mA cm^{-2} for Ni^{2+}/birnessite with increasing electrochemical cycles. (Adapted with permission (ref. 110) Copyright Wiley and Sons (2016).)

Ni^{2+} MnO_2 catalyst exhibiting an overpotetnial at 10 mA cm^{-2} of 400 mV.[110] This is a significant increase in activity when compared to the bare MnO_2 as a 350 mV difference is observed. This synthetic route should be exploited using other OER catalysts as inserting other transition metal ions, *e.g.* Ni^{2+}, into the interlayer spaces of layered TMOs may be way of promoting the activity of these materials. Anion exchange is already utilised in research for enhancing electrocatalytic performance of layered TMOs, but the anions used are not currently based on other transition metals, *e.g.* Ni^{2+}, that are known to be active for the OER.[54]

The majority of layered TMO materials which undergo anion exchange consist of more than one metal therefore this section of the review will focus on bi- and tri-metal TMOs. Recently, in a research setting, NiFe based hydroxides/oxides have emerged as a cheap alternative for the OER in alkaline media compared to PGM based oxides *i.e.* RuO_2 and IrO_2. These materials also exhibit a layered structure, with some research groups having exploited this by changing the interlayer spacings of the NiFe by anion exchange.

For example, layered $Ni_{0.8}Fe_{0.2}OH$ LDH prepared by a hydrothermal synthesis was subjected to anion exchange, using BO_3^{3-} ions, resulted in an increased in the interlayer spacing from 5.4 Å to 6.2 Å.[111] The anion exchange process introduced a boost in the LDH specific surface area from 150.9 m^2 g^{-1} to 170.9 m^2 g^{-1} which was determine by BET analysis. Additionally the OER properties of the layered $Ni_{0.8}Fe_{0.2}OH$ LDH in 1 M KOH were clearly enhanced after anion exchange as the overpotential at 10 mA cm^{-2} and the Tafel slope values both improved. The overpotetnial and Tafel slope value increase by *ca.* 50 mV and 25 mV, respectively, for the BO_3^{3-} treated material compared to the bare LDH. This enhancement in the OER catalytic activity of the layered $Ni_{0.8}Fe_{0.2}OH$ LDH was correlated with the increase in the interlayer spacing exposing more active sites due to the anion exchange process. In this study, it was suggested that the O_2 mechanism of the borate intercalated LDH was enhanced compared to the bare LDH due to the borate ions acting as a proton accepting agent which increases the O–O bond formation during the OER.[111]

Another recent study on the OER properties of an anodic borate doped $Ni(OH)_2$ has also indicated that the presence of borate enhances the proton accepting properties during the OER compared to a non-doped $Ni(OH)_2$ catalyst, Fig. 11(A and B).[112] The overpotential of the borate doped Ni catalyst is increased at 10 mA cm^{-2} compared to the non-doped Ni material. However, as the Tafel slope values are similar the mechanism in which the OER proceeds is assumed to be the same; the rate determining step involves the formation of adsorbed peroxide intermediates (–OOH). Therefore, the enhancement in the OER was attributed to the reversible transformation of the BO_3^{3-} to a BO_3^{3}-OH. The presence of the four coordinated borate was confirmed by NMR spectroscopy. This BO_3^{3}-OH can accept a proton from the Ni–O–OH_2 intermediate and subsequently release H_2O, and an electron, leaving a Ni-OOH site.[112] This step may require less energy to proceed compared to the equivalent step during the O_2 generation of the bare $Ni(OH)_2$, Fig. 11(C), resulting in the enhanced activity, Fig. 11(D).

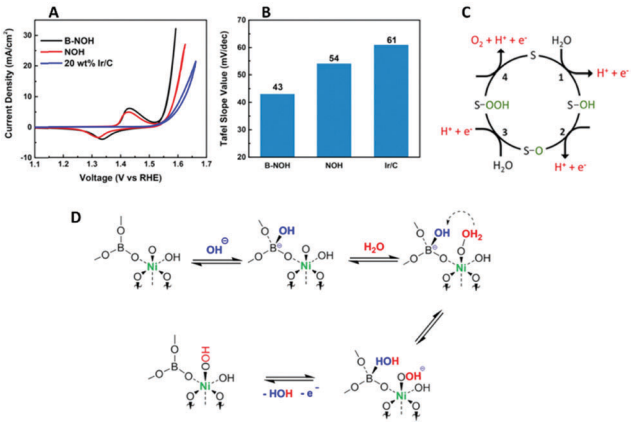

Fig. 11 (A) iR-corrected cyclic voltammograms of OER on B-NOH, NOH, and Ir/C (B) comparison of Tafel slopes (C) the PCET mechanism of OER in the literature. "S" represents a surface site and (D) the proposed rate determining step (RDS) on a borate-coordinated Ni active center. (Adapted with permission (ref. 112) Copyright American Chemical Society (2018).)

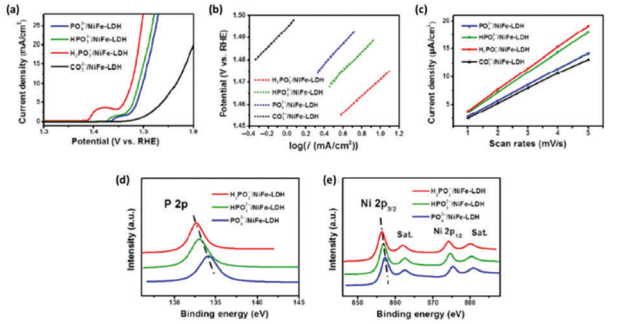

Fig. 12 (a) Polarisation curves of four LDH catalysts (PO_4^{3-}/NiFe-LDH, HPO_3^{2-}/NiFe-LDH, $H_2PO_2^{-}$/NiFe-LDH, and CO_3^{2-}/NiFe-LDH); $H_2PO_2^{-}$/NiFe-LDH shows the lowest onset potential and fastest current density increase; (b) Tafel plots, (c) C_{dl} calculations for the four catalysts. XPS data of the PO_4^{3-}/NiFe-LDH, HPO_3^{2-}/NiFe-LDH, and $H_2PO_2^{-}$/NiFe-LDH: (d) P 2p and (e) Ni 2p spectra. (Adapted with permission (ref. 114) Copyright Springer (2017).)

By comparing recent studies, it has been further shown that the absolute OER overpotentials of NiFe LDH based catalysts fluctuate depending on the ions utilised during the anion exchange process.[113] Similarly to the previous study on intercalated NiFe with BO_3^{3-} ions, the OER performance of a NiFe LDH intercalated with Mo ions during anion exchange, also exhibited a more cathodic behavior favoring the OER.[111] For this particular study, the OER optimisation as a result of the anion exchange process was clear as the overpotential at 10 mA cm^{-2} for the NiFe Mo treated LDH increased by 35 mV compared to the untreated NiFe LDH. The authors attributed this observation to an increase in the electrochemical active sites as a result of the ultrathin thickness of the anion exchanged NiFe LDH.

More interestingly when comparing the two aforementioned studies, the choice of ion for the anion exchange process is evidently important in terms of the resulting electrochemistry. The two previous works use different layer intercalating anions, *e.g.* Mo or BO_3^{3-} ions, in the anion exchange process but a similar hydrothermal synthetic route to make the NiFe LDHs. Therefore it can be noted that the OER activity changes depending on the ion utilised. The OER overpotentials for the BO_3^{3-} ion intercalated NiFe LDH exhibited a larger increase when compared to the Mo ions; a difference of 50 mV was observed for the borate intercalated material and only 35 mV for the Mo intercalated material when compared to their relevant untreated counterpart. Perhaps indicting the BO_3^{3-} ions may be a more suitable choice of anion over Mo ions for the anion exchange process for NiFe based materials.

Furthermore, the OER activity of the NiFe LDH can be readily tuned by adopting different phosphorus based anions; phosphate, phosphite and hypophosphite, during the anion exchange process of an carbonate intercalated NiFe LDHs.[114] The OER performance of the NiFe LDH reveals that the choice of intercalation anion has an effect on the electrocatalytic performance, Fig. 12(a–c). From the LSV curves, Fig. 12(a), it is evident that the phosphorous based anions significantly improves the OER when compared to the carbonate intercalated NiFe LDH, however the Tafel slope was not affected; indicating that O_2 evolution proceeds by the same mechanism for all of the NiFe LDH, Fig. 12(b). Interestingly, the electrochemical surface area (ECSA), Fig. 12(c), exhibited the same trend to the overpotential values at 10 mA cm^{-2} *i.e.* the hypophosphite NiFe showed the best OER overpotentials and the highest ECSA, followed by the phosphite NiFe, then the phosphate NiFe and, finally, the carbonate NiFe.

The rationale for the trend observed for the NiFe LDH based phosphorus catalysts originates from a previous observation that the OER activity of NiFe based catalysts is strongly influenced by the Ni sites.[115] From XPS analysis, Fig. 12(d and e), it is clear the lowest Ni valence states are present for the NiFe/hypophosphite and can be correlated to this anion ($H_2PO_2^{-}$) possessing the strongest reducibility compared to the other anions. Hence, more electron rich Ni sites would be available for oxidation during the OER *i.e.* more active sites.

Additionally, the $H_2PO_2^{-}$ NiFe possess the largest ECSA/double layer capacitance value of 3.8 μF cm^{-2} when compared to 3.2 and 3.6 μF cm^{-2} for the PO_4^{3-} and the HPO_3^{2-} NiFe based LDH, respectively. This is an interesting example of when the OER activity of a material (NiFe LDH) can be tuned for the OER by using various anions in the synthetic process.

In the literature, it has been shown that a combination of both anion exchange and liquid phase exfoliation can improve the oxygen evolution properties of various bi-metallic LDH materials such as CoCo, NiCo and NiFe LDHs when compared to its bulk LDH and to the state-of-the-art IrO_2 for OER.[67] Unlike other studies previously mentioned in this review, this work utilised anion exchange as a pre-conditioning step before the exfoliation of the 2D materials by liquid phase exfoliation, rather than the main treatment step. The anion exchange process facilitates the delamination of the 2D structures during the exfoliation process as the interlayer spacings were increased prior to exfoliation.

The anion exchange process was carried on the topochemical fabricated CoCo and NiCo LDH by exchanging the Br^{-} ions

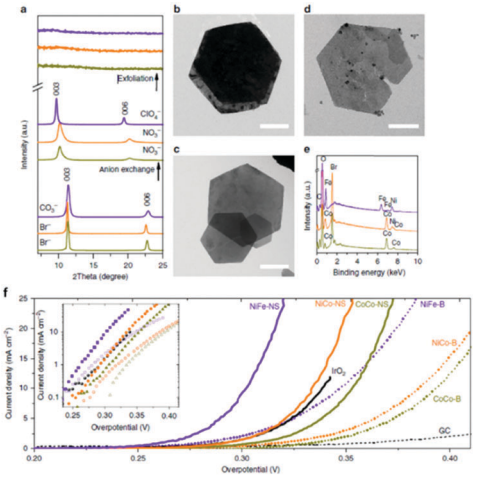

Fig. 13 (a) XRD spectra. (b–d) TEM images of (b) CoCo LDH–Br. Scale bar, 1 mm. (c) NiCo LDH–Br. Scale bar, 1 mm. (d) NiFe LDH–CO_3^{2-}. Scale bar, 150 nm. (e) Energy-dispersive X-ray spectra. CoCo LDH: yellow-green lines; NiCo LDH: orange lines; NiFe LDH: purple lines. (f) Polarization curves. Inset shows the Tafel plots. Scan rate was 5 mV s^{-1}. The loading was about 0.07 mg cm^{-2} for LDH materials and 0.21 mg cm^{-2} for IrO_2 nanoparticles. (Reproduced with permission (ref. 67) Copyright Nature Publishing Group (2014).)

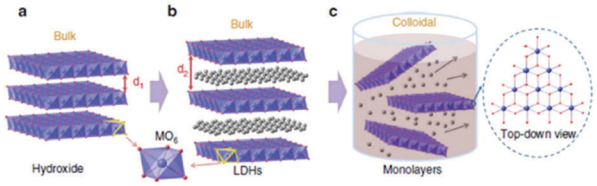

Fig. 14 Schematic representation of materials' structures. (a) Layered hydroxides. d_1 is the inter-layer distance of the hydroxide. (b) LDHs with inter-layer anions and water molecules. d_2 is the inter-layer distance of the LDHs. (c) Exfoliated LDH monolayers dispersed in a colloidal solution. Each single layer is composed of edge-sharing octahedral MO_6 moieties (M denotes a metal element). Metal atoms: purple spheres; oxygen atoms: red spheres; inter-layer anions and water molecules: grey spheres. Hydrogen atoms are omitted. (Reproduced with permission (ref. 67) Copyright Nature Publishing Group (2014).)

with NO^{3-} ions and for the hydrothermally produced NiFe by switching the CO_3^- ions with ClO_4^- ions which was successful tracked by XRD Fig. 13(a) and imaged by TEM-EDX, Fig. 13(b–e). The interlayer spacing of the CoCo and NiCo increase from 7.8 Å to 8.7 Å, while the initial interlayer spacing of the NiFe LDH increased from 7.7 Å to 9.1 Å. Subsequently, the chemical composition and morphology of the initial LDHs were maintained. Liquid phase exfoliation was subsequently carried out on the LDH to form 2D structures and was confirmed by a combination of using the Tyndall effect to prove the colloidal nature of the exfoliated suspension, the determination of the 2D layers by TEM analysis, and the absence of the diffraction peaks in the XRD analysis, Fig. 13(a), when compared to the bulk LDHs.

The OER performance of the bulk and exfoliated LDHs were determined in 1 M KOH and subjected to the same experimental conditions and can be seen in Fig. 13(f). The results show that all of the exfoliated LDH was significantly enhanced when compared to their bulk counterpart in respect to the measured overpotetnial at a current density of 10 mA cm^{-2}. The NiCo and NiFe also out-performed IrO_2; a state-of-the-art OER catalyst.

The authors attribute the dramatic difference in activity to a greater exposure of the MO_6 sites after exfoliation, see Fig. 13. It is evident, that these MO_6 sites are the active site for OER in these LDH materials therefore a greater number of these sites will be readily accessible during water oxidation when compared to the bulk LDH, where a portion of these MO_6 sites will be blocked by the charge neutralising anion between the 2D layers (Fig. 14). Furthermore, it is quite clear that this increase in activity is due to the rise in active site density and not due to a change in the ECSA as the increase in the ECSA 2D materials is not sufficient to explain the improvement seen in the OER performance.

Selecting the appropriate trivalent ion during the synthetic procedure for a LDH is essential to improve the performance of the catalyst for OER. Recently, multiple studies have emerged that highlights the advantage of fabricating LDH with Fe^{3+} as the trivalent species over Al^{3+} ions for the OER.[116,117] One particular study, that co-precipitates various CoFe and CoAl LDHs with different percentages of a Fe trivalent ion from 15 to 45% in relation to the divalent ions, reports that not only does increasing the amounts of Fe enhance, to 35%, the CoFe LDH towards the OER but the addition of subsequent amounts of Al to the Co for the CoAl LDH suppresses the OER activity, Fig. 15.[117] The reason for the enhancement for the CoFe with increase amounts of Fe^{3+} is not pin-pointed by the authors experimentally but is rationalised by theories expressed by other groups, which suggests the Fe^{3+} is the active site for the OER and the Co^{2+} is acting as a host material.[118] Furthermore, the authors proposed the OER mechanism on the CoFe LDH proceeds at lower potentials compared to a Co only material due to substitution of the Co sites with Fe sites. This is based on a previously reported Co OER mechanism which states that at high OER potentials the Co^{4+} ion, bonded to oxo groups, is a vital intermediate for active Co OER catalysts.[119] The Co^{4+} promotes the proton coupled electron transfer (PCET) step resulting in the formation of the O radicals on the Co^{3+} sites before the rate determining step and the generation of O_2. However, in the case of the CoFe LDH, when Fe ions is substituted for some of the Co sites, this PCET step takes place on Fe^{4+}, as Fe is believed to be oxidised at lower potentials, enhancing the OER activity.[117]

Finding the true reason for the enhanced catalytic effect of LDH materials when Fe^{3+} is utilised as the trivalent ion could lead to better and more active OER catalysts as the fabrication of LDH materials could be specifically designed to mimic these findings.

This study and all of the previously highlighted reports in this review, summarised in Table 2, show that the fabrication of LDH from the choice of trivalent ions to the treatments (anion exchange or exfoliation to 2D phase) applied after synthesis are critical to the performance of these materials as OER catalysts. It is evident that aforementioned treatments greatly improve

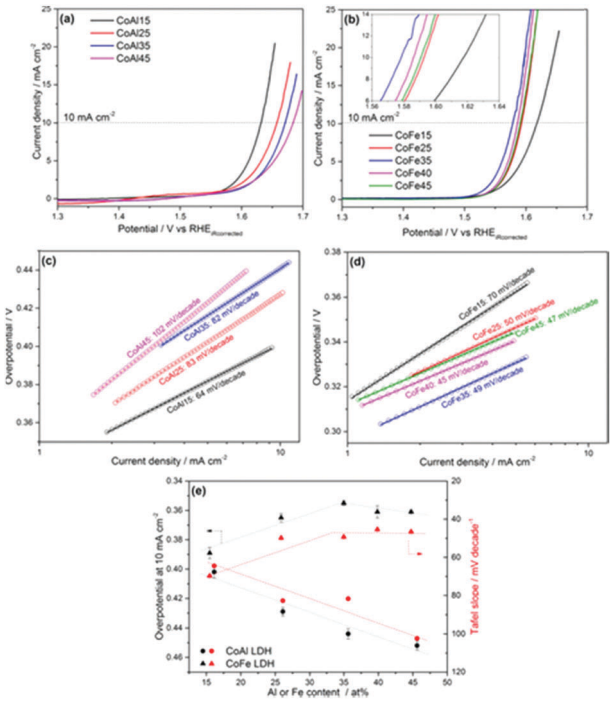

Fig. 15 OER activities of the (a) CoAl and (b) CoFe samples; Tafel slopes of the (c) CoAl and (d) CoFe samples; (e) overpotential at 10 mA cm^{-2} and Tafel slopes of the catalysts *versus* Al/Fe atomic content, as determined by ICP-OES. (Reproduced with permission (ref. 117) Copyright Wiley and Sons (2017).)

the OER properties of the 'bare' LDH and more studies into these fabrication methods will undoubtedly see a further increase over the next number of years. These advances could provide an avenue to discover a cheap and active catalyst based on an LDH materials for electrolysis. This would greatly benefit the current energy crisis in finding an alternative energy conversion catalyst as an alternative to fossil fuels.

Oxygen reduction reaction (ORR)

Recently, various reports on the ORR and the use of layered transition metal oxide catalysts have emerged. Similar to the OER, post-fabrication treatment of these layered TMO based materials can also show enhancements toward the ORR, see Table 3. For example MnO_2 layered nanosheet materials exhibited improved ORR activity after a so called 'sulfurisation process'. This MnO_2 based nanosheet was prepared by adding $KMnO_4^-$ into a solution of graphene oxide and water at 80 °C and mixed for 24 hours.[74] The product was filtered, washed and dried, then subjected to the 'sulfurisation process'. This entailed mixing sulfur powder with the layered MnO_2 nanosheet product in a crucible and exposing the powder mixture to 155 °C to introduce nanosize pores into the MnO_2 nanosheets, see Table 1 for more details and Fig. 16(a) for fabrication schematic.

The ORR performance, Fig. 16(b), reveals that the post-fabrication sulfurisation process improved its catalytic activity; $E_{1/2}$ *vs.* RHE by 40 mV. The $E_{1/2}$ *vs.* RHE values for the pre-treated and nonporous MnO_2 sheets were 0.69 and 0.73 V, respectively. Interestingly, the nanoporous MnO_2 nanosheets is only a mere 100 mV less than Pt/C, the optimum ORR catalysts currently used in fuel cells. The improvement in the ORR activity was related, by the authors, to the evidence observed by the XPS analysis which indicated that more oxygen vacancies where present for the post treated MnO_2, Fig. 16(c). The oxygen vacancies may help to facilitate oxygen absorption and reduce kinetic barriers by exposing the Mn sites which was induced by the post synthetic sulfurisation step. This report illustrated that a simple post-fabrication step can help enhance the ORR performance of a mono-metallic LDH and can be easily adapted in future studies by others.

We have already shown previously in this review that NiFe LDHs are researched extensively for the OER however, NiFe LDH based materials have also been explored in the literature as a catalyst for the ORR.[120] Herein, we will show how simple modification of these NiFe LDH can change the ORR performance of these popular LDH. The addition of both graphene and rGO during the fabrication method can alter the ORR response of NiFe LDH materials. In one particular study, 'bare' NiFe was produced by a one-pot solvothermal synthesis and the graphene oxide was obtained by using the well-known Hummer method.[121,122] Subsequently, to fabricate the NiFe/rGO, the graphene oxide was also added to the Teflon reactor with the Ni and Fe metal salts for solvothermal synthesis.

After which, the product was subjected to hydrazine hydrate and ammonia for 1 hour at 90 °C in order to allow for the graphene oxide to be reduced. The NiFe/GO catalysts was prepared in the same manner but the reduction step was omitted.[120] The authors examined the ORR properties of these three NiFe based materials in 1 M KOH and by using a high surface area Ni foam support. The ORR activity increase with the addition of the graphene oxide to the NiFe which further increases when rGO is substituted for the graphene oxide. The improved activity of the NiFe/rGO was a result of more exposed active ORR sites which arose from the strong interactions between the NiFe LDH and the rGO observed from XRD analysis.

Another interesting fabrication concept leading to an enhancement in ORR regarding NiFe based LDHs involves the anchoring of NiFe LDH onto N-doped graphene-like 3D macro–meso-porous carbon (denoted as nNiFe LDH/3D MPC).[123] The fabrication technique consisted of two steps; the first step was the anchoring of the metal salt precursors onto the 3D MPC platform then growth of the NiFe LDH by a co-precipitation method, see Fig. 17(a). The authors proposed that the carbon based platform would promote the activity of the NiFe towards ORR by manipulating defect sites which would increase the catalytic activity of the overall material.

The ORR performance of the nNiFe LDH/3D MPC was also compared to the 3D MPC platform and a NiFe LDH catalyst with the 3D MPC added after synthesis. The ORR performance of the nNiFe LDH/3D MPC was indeed better than the bNiFe LDH + 3D MPC, again indicating that the route taken to yield LDH catalysts for the ORR have a significant influence upon it's

Table 2 Summary of the OER TMO catalysts with respect to the intrinsic properties relating to the increase in OER, their structures and OER overpotential (V) at 10 mA cm^{-2}

Material	Intrinsic properties related to increase in OER activity as reported in the relevant study	Structure of catalysts	OER overpotential (V) at 10 mA cm^{-2}	Ref.
$Ni(OH)_2$	The authors suggest that the $Ni(OH)_2$ which was electrochemically activated has been converted into the more OER active NiOOH phase.	2D	*ca.* 0.38	78
$Ni(OH)_2$ electrochemically activated		2D	*ca.* 0.35	78
$Co(OH)_2$	The smallest $Co(OH)_2$ NS exhibited the best OER activity due to their high edge content compared with the bulk $Co(OH)_2$ and the larger $Co(OH)_2$ NS. The electrically and mechanical properties of the catalyst was enhanced by adding CNT which increased the OER activity of the $Co(OH)_2$ NS materials.	Brucite	0.45	76
$Co(OH)_2$ NS		2D	0.33	76
$Co(OH)_2$ NS with 10 wt% CNT		2D	0.29	76
δ-MnO_2	The increase in the OER performance of the exfoliated δ-MnO_2 was rationalised by the increase in the electrochemical surface area.	Birnessite	Did not reach 10 mA cm^{-2}	104
δ-MnO_2 exfoliated		Birnessite	0.32	104
Bare MnO_2	The authors suggests that the increasing presence of $Ni(OH)_2$ increases the OER activity due to the tighter confinement of the $Ni(OH_2)$ in the birnessite interlayers which increases the orientation of the water molecules, promoting the OER.	Birnessite	0.75	110
MnO_2 with 6.1% Ni		Birnessite	0.43	110
MnO_2 with 6.5% Ni		Birnessite	0.40	110
MnO_2 with 7.7% Ni		Birnessite	0.40	110
$Ni_{0.8}Fe_{0.2}OH$	The increase in the activity of the NiFe based LDH intercalated with borate was attributed to the increase in the specific surface area which in turn increased the mass transport and charge transfer properties compared to the NiFe which was not intercalated with borate ions.	Hydrotalcite	0.35	111
$Ni_{0.8}Fe_{0.2}OH$ intercalated with BO_3^{3-}		Hydrotalcite	0.27	111
$Ni(OH)_2$	The ECSA measurements of the bare and doped $Ni(OH)_2$ revealed that the ECSA was the same. The authors concluded that the borate groups enhances the PCET.	Brucite	0.37	112
$Ni(OH)_2$ doped with BO_3^{3-}		Brucite	0.32	112
NiFe LDH	The NiFe–Mo LDH exhibited a higher availability of electrochemical active sites which the authors correlated with the increase in the OER compared to the NiFe LDH.	Hydrotalcite	>0.28	113
NiFe LDH intercalated with Mo ions		Hydrotalcite	0.27	113
NiFe intercalated with PO_4^{3-}	The lowering of the Ni valence state by the phosphorus based ions results in the increased availability of electron rich Ni sites for the OER.	Hydrotalcite	0.27	114
NiFe intercalated with HPO_3^{2-}		Hydrotalcite	0.25	114
NiFe intercalated with $H_2PO_2^-$		Hydrotalcite	0.23	114
NiFe intercalated with CO_3^{2-}		Hydrotalcite	0.35	114
CoCo bulk	The increase in OER activity from the bulk to the NS materials attributed to the increase in active site density and conductivity of the NS materials.	Hydrotalcite	0.39	67
NiCo-bulk		Hydrotalcite	0.38	67
NiFe-bulk		Hydrotalcite	0.35	67
CoCo NS		2D	0.35	67
NiCo NS		2D	0.33	67
NiFe NS		2D	0.30	67
CoAl 15	The presence of Al ions in the LDH structure decreases activity.	Hydrotalcite	0.40	117
CoAl 25		Hydrotalcite	0.43	117
CoAl 35		Hydrotalcite	0.44	117
CoAl 45		Hydrotalcite	0.45	117
CoFe 15	Substitution of Fe ions for the Co ions in the LDH structure which ultimately leads to a Fe^{4+} site facilitating the PCET to the Co^{3+} sites during the OER.	Hydrotalcite	0.39	117
CoFe 25		Hydrotalcite	0.37	117
CoFe 35		Hydrotalcite	0.36	117
CoFe 40		Hydrotalcite	0.37	117
CoFe 45		Hydrotalcite	0.365	117

Table 3 Summary of the ORR TMO catalysts with respect to the intrinsic properties relating to the increase in ORR, their structures and ORR activity

Material	Intrinsic properties related to increase in ORR activity as reported in the relevant study	Structure of catalysts	ORR $E_{1/2}$ potential (V) *vs.* RHE or trend in activity in relevant study	Ref.
MnO_2	Increase in oxygen vacancies.	Birnessite	0.69	74
Porous MnO_2		Birnessite	0.73	74
NiFe LDH with graphene oxide (GO)	Increase in ORR sites due to strong interactions between the NiFe and the rGO compared to the NiFe and the GO.	Hydrotalcite	NiFe with the rGO outperformed the NiFe with GO.	120
NiFe LDH with reduced graphene oxide (rGO)		Hydrotalcite		120
NiFe on N-doped graphene-like 3D macro–meso-porous carbon	None suggested by authors.	Hydrotalcite	NiFe fabricated directly on the N-doped graphene-like carbon during fabrication outperformed the NiFe mixed with the carbon post fabrication.	123
NiFe mixed with NiFe N-doped graphene-like 3D macro–meso-porous carbon		Hydrotalcite		123
CoNiFe (Co : Ni = 67 : 33) (M1)	The optimum ORR activity of the M3 catalysts was attributed to the increase in oxygen vacancies due to the higher amount of NiO and octahedral Co^{3+} sites in the spinal structure of the M3 material compared to the M1 and M2 catalysts.	Hydrotalcite	M3 > M1 > M2	124
CoNiFe (Co : Ni = 73 : 27) (M2)		Hydrotalcite		124
CoNiFe (Co : Ni = 57 : 43) (M3)		Hydrotalcite		124
PPy/rGO	The authors reported synergistic effects for the enhanced ORR activity of the CoNiMn–PPy/rGO catalyst.	n/a	CoNiMn–PPy/rGO > CoNiMn–rGO > PPy/rGO	125
CoNiMn–rGO		Hydrotalcite		125
CoNiMn–PPy/rGO		Hydrotalcite		125

Fig. 16 (a) Schematic diagram for the synthesis of np-MnO_2-ns and (b) ORR performance of carbon, MnO_2-ns, np-MnO_2-ns, and 20 wt% Pt/C in O_2-saturated 0.1 M KOH aqueous solution at room temperature, LSV measured at 5 mV s^{-1} and 1600 rpm and (c) XPS curves for the MnO_2-ns and np-MnO_2-ns materials. (Reproduced with permission (ref. 74) Copyright Wiley and Sons (2018).)

Fig. 17 (a) Schematic illustration of the synthesis of nNiFe LDH/3D MPC and (b) ORR LSV curves for *n*NiFe LDH/3D MPC, bNiFe LDH + 3D MPC and 3D MPC in 0.1 M KOH at a scan rate of 5 mV s^{-1} with a rotation speed of 900 rpm. (Reproduced with permission (ref. 123) Copyright Royal Society of Chemistry (2018).)

catalytic properties, Fig. 17(b). Unfortunately, and also stated by the authors, the LDH based materials under-performed when compared to the 3D MPC platform. Perhaps with further aids, such as CNT or other conductive aids, this NiFe based LDH could achieve better ORR potentials.

The use of ternary metal LDH catalysts for the ORR have been explored. Two studies based on different ternary LDH catalysts are reviewed herein to highlight the effect of the fabrication techniques on these ternary LDH materials toward the ORR.[124,125] In the first study, the effect of varying the molar ratio of two of the three metals present in a CoNiFe material on the ORR was investigated. In this study, three CoNiFe LDHs was synthesis by a two-step method involving a co-precipitation process and then a thermal annealing process. During the

fabrication procedure the molar ratio of the Co^{2+} : Ni^{2+} (Ni^{2+} molar percentages (sample name): 33% (M1), 27% (M2) and 47% (M3)) was varied and the molar percentage of the Fe^{3+} remained constant and as a result a reverse spinel structure for all of the CoNiFe LDH catalysts were produced. The ORR activity of the three CoNiFe LDH materials were probed on a GC disk in 0.5 M KOH. The ORR evaluation revealed a trend with respect to the percentage of Ni^{2+} in the LDH; the larger percentage of Ni^{2+} yielded the best performing catalysts while the smallest amount of Ni^{2+} (or the largest amount of Co^{2+}) produced the worst ORR catalyst. Hence the trend observed toward the ORR performance of the catalysts, from best to worst, is M3 < M1 < M2. XPS analysis provided a rational explanation for this outcome; the authors correlated the higher amount of NiO and octahedral Co^{3+} sites in the spinal structure of the M3 material to be the cause of the increased ORR activity *i.e.* the active ORR site. The authors suggested that this result indicates more oxygen vacancies are present on the surface of the material for ORR to proceed when compared to the M2 and M1 materials as these materials contained less NiO/Co^{3+} sites. This study suggests that approx. a 50 : 50 ratio of Ni : Co is optimum in the ternary CoNiFe LDH is optimum for the ORR.

In the second study, a similar co-precipitation fabrication process to produce the ternary metal LDH materials was utilised compared to the aforementioned study however this time a CoNiMn LDH based catalysts was fabricated. Additionally this work set out to investigate the effect induced by reduced graphene oxide and poly-pyrrole on the CoNiMn LDH towards ORR.[125] The reduced graphene oxide (rGO) component of the composite LDH material was prepared by the Hummers method while the poly-pyrrole was fabricated by polymerising pyrrole. Subsequently, the Co, Ni and Mn metal salts were then added to the rGO in deionised water and finally the poly-pyrrole (PPY). To produce the composite LDH the three components were added together with NaOH to induce a co-precipitation reaction, the composite was then aged for 24 hours under stirring, Fig. 18(a). Additionally, for comparison a PPy/rGO, a CoNiMn–rGO and a CoNiMn-LDH were also fabricated by this method; with the missing component in the materials name omitted from the fabrication route.

The ORR performance of the CoNiMn–PPy/rGO, PPy/rGO, and CoNiMn–rGO was evaluated alongside state of the art ORR materials, Fig. 18(b). The CoNiMn–rGO mixed with the PPy/rGO post fabrication was also evaluated to determine if the presence of the PPy/rGO was enough to effect the ORR activity of the LDH or if the PPy/rGO needed to be fabricated directly with the LDH. The results showed that the CoNiMn–PPy/rGO LDH composite made directly during synthesis out-performed all of the aforementioned materials with an $E_{1/2}$ value *vs.* RHE of ~0.78 V in 0.1 M KOH. Additionally, the CoNiMn–PPy/rGO LDH composite proved to be a better ORR catalyst than the more expensive and PGM based RuO_2/C however, yet again, the state-of-the-art ORR material, Pt/C, was the optimum catalyst. Interesting, the CoNiMn–rGO mixed with the PPy/rGO post fabrication exhibits a huge decrease in its $E_{1/2}$ value. This study indicates that the fabrication of the composite *in situ* or post fabrication changes the properties associated with the ORR and that the synthesis of the CoNiMn–PPy/rGO LDH composite in a one-pot synthesis

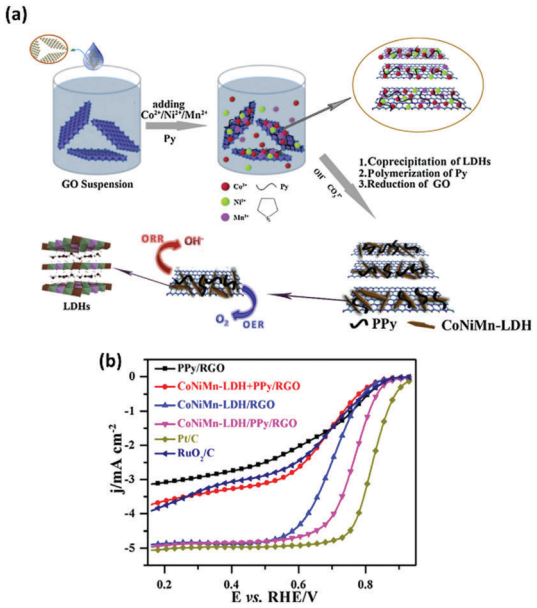

Fig. 18 (a) Schematic illustration of fabrication process towards CoNiMn-LDH/PPy/RGO for oxygen reduction reaction and (b) LSV curves of the four samples, 20 wt% Pt/C, and 20 wt% RuO_2/C catalyst at 1600 rpm in O_2-saturated 0.1 M KOH. (Reproduced with permission (ref. 125) Copyright Elsevier (2017).)

creates synergistic effects toward the ORR which are not observed for the CoNiMn–rGO mixed with the PPy/rGO.

Conclusion and outlook

There has been a significant increase in the utilisation of LDHs as electrocatalysts for O_2 electrode reactions; the OER and ORR, in alkaline electrolyte in the recent years. It is clear from this review that even small quantities of simple additives, *i.e.* rGO or CNTs, during the synthetic process, the use of high surface area supports and/or exfoliation of these layered materials changes the resulting catalytic properties. As observed from the various articles reviewed here, these modifications during the synthesis of the LDHs/LDH-based composites can propel the activity exhibited close to the expensive and scarce state-of-the-art catalysts *e.g.* RuO_2 for OER and Pt for ORR. Further research into the optimisation and/or modification of these interesting materials may open avenues to lead the scientific community in finding a promising cheap and highly active materials for the two aforementioned O_2 reactions; a vital step towards the efficient running of a future hydrogen economy.

Conflicts of interest

There are no conflicts to declare.

Acknowledgements

This work emanated from financial support from the Advanced Functional Nanorobots project (reg. no. CZ.02.1.01/0.0/0.0/15_003/0000444 financed by the EFRR). M. P. B. would also

like to acknowledge the European Structural and Investment Funds, OP RDE-funded project 'ChemJets' (No. CZ.02.2.69/0.0/0.0/16_027/0008351). Z. S. was supported by Czech Science Foundation (GACR No. 17-11456S) and by the financial support of the Neuron Foundation for science support.

Notes and references

1 I. E. Agency, 2017.
2 K. Harrison and J. I. Levene, *Solar Hydrogen Generation: Toward a Renewable Energy Future*, 2008.
3 S. Shafiee and E. Topal, *Energy Policy*, 2009, **37**, 181–189.
4 I. Dincer and C. Acar, *Int. J. Hydrogen Energy*, 2015, **40**, 11094–11111.
5 R. Subbaraman, D. Tripkovic, K.-C. Chang, D. Strmcnik, A. P. Paulikas, P. Hirunsit, M. Chan, J. Greeley, V. Stamenkovic and N. M. Markovic, *Nat. Mater.*, 2012, **11**, 550.
6 A. Faur Ghenciu, *Curr. Opin. Solid State Mater. Sci.*, 2002, **6**, 389–399.
7 M. S. Dresselhaus and I. L. Thomas, *Nature*, 2001, **414**, 332–337.
8 G. Merle, M. Wessling and K. Nijmeijer, *J. Membr. Sci.*, 2011, **377**, 1–35.
9 K. V. Lykhnytskyi, *Hydrogen Materials Science and Chemistry of Carbon Nanomaterials*, Springer Netherlands, Dordrecht, 2007.
10 J. Chi and H. Yu, *Chin. J. Catal.*, 2018, **39**, 390–394.
11 M. E. G. Lyons, R. L. Doyle, D. Fernandez, I. J. Godwin, M. P. Browne and A. Rovetta, *Electrochem. Commun.*, 2014, **45**, 60–62.
12 D. E. Hall, *J. Electrochem. Soc.*, 1983, 317–321.
13 H. Tributsch, *Int. J. Hydrogen Energy*, 2008, **33**, 5911–5930.
14 K. Zeng and D. Zhang, *Prog. Energy Combust. Sci.*, 2010, **36**, 307–326.
15 C. C. L. McCrory, S. Jung, I. M. Ferrer, S. M. Chatman, J. C. Peters and T. F. Jaramillo, *J. Am. Chem. Soc.*, 2015, **137**, 4347–4357.
16 C. C. L. McCrory, S. Jung, J. C. Peters and T. F. Jaramillo, *J. Am. Chem. Soc.*, 2013, **135**, 16977–16987.
17 C. L. Manzanares Palenzuela, J. Luxa, Z. Sofer and M. Pumera, *ACS Appl. Mater. Interfaces*, 2018, **10**, 17820–17826.
18 I. Roger and M. D. Symes, *J. Mater. Chem. A*, 2016, **4**, 6724–6741.
19 M. S. Burke, S. Zou, L. J. Enman, J. E. Kellon, C. A. Gabor, E. Pledger and S. W. Boettcher, *J. Phys. Chem. Lett.*, 2015, **6**, 3737–3742.
20 M. Schalenbach, A. R. Zeradjanin, O. Kasian, S. Cherevko and K. J. J. Mayrhofer, *Int. J. Electrochem. Sci.*, 2018, **13**, 1173–1226.
21 K. J. Seong, K. Byunghoon, K. Hyunah and K. Kisuk, *Adv. Energy Mater.*, 2018, **8**, 1702774.
22 M. G. Walter, E. L. Warren, J. R. McKone, S. W. Boettcher, Q. Mi, E. A. Santori and N. S. Lewis, *Chem. Rev.*, 2010, **110**, 6446–6473.
23 M. E. G. Lyons, R. L. Doyle, M. P. Browne, I. J. Godwin and A. A. S. Rovetta, *Curr. Opin. Electrochem.*, 2017, **1**, 40–45.
24 T. Sinigaglia, F. Lewiski, M. E. Santos Martins and J. C. Mairesse Siluk, *Int. J. Hydrogen Energy*, 2017, **42**, 24597–24611.
25 A. Demirbas, *Energy Sources, Part B*, 2017, **12**, 172–181.
26 T. da Silva Veras, T. S. Mozer, D. da Costa Rubim Messeder dos Santos and A. da Silva César, *Int. J. Hydrogen Energy*, 2017, **42**, 2018–2033.
27 X. J. Chua, J. Luxa, A. Y. S. Eng, S. M. Tan, Z. Sofer and M. Pumera, *ACS Catal.*, 2016, **6**, 5724–5734.
28 K. A. Stoerzinger, L. Qiao, M. D. Biegalski and Y. Shao-Horn, *J. Phys. Lett.*, 2014, **5**, 1636–1641.
29 R. R. Rao, M. J. Kolb, N. B. Halck, A. F. Pedersen, A. Mehta, H. You, K. A. Stoerzinger, Z. Feng, H. A. Hansen, H. Zhou, L. Giordano, J. Rossmeisl, T. Vegge, I. Chorkendorff, I. E. L. Stephens and Y. Shao-Horn, *Energy Environ. Sci.*, 2017, **10**, 2626–2637.
30 Y. Lee, J. Suntivich, K. J. May, E. E. Perry and Y. Shao-Horn, *J. Phys. Lett.*, 2012, **3**, 399–404.
31 M. Escudero-Escribano, A. F. Pedersen, E. A. Paoli, R. Frydendal, D. Friebel, P. Malacrida, J. Rossmeisl, I. E. L. Stephens and I. Chorkendorff, *J. Phys. Chem. B*, 2018, **122**, 947–955.
32 M. E. G. Lyons, R. L. Doyle, D. Fernandez, I. J. Godwin, M. P. Browne and A. Rovetta, *Electrochem. Commun.*, 2014, **45**, 56–59.
33 Z. Zhao, H. Wu, H. He, X. Xu and Y. Jin, *Adv. Funct. Mater.*, 2014, **24**, 4698–4705.
34 Z.-Y. Yu, C.-C. Lang, M.-R. Gao, Y. Chen, Q.-Q. Fu, Y. Duan and S.-H. Yu, *Energy Environ. Sci.*, 2018, **11**, 1890–1897.
35 L. Wang, T. Du, J. Cheng, X. Xie, B. Yang and M. Li, *J. Power Sources*, 2015, **280**, 550–554.
36 Y. Liang, Q. Liu, A. M. Asiri and X. Sun, *Electrochim. Acta*, 2015, **153**, 456–460.
37 B. Zhang, X. Zheng, O. Voznyy, R. Comin, M. Bajdich, M. García-Melchor, L. Han, J. Xu, M. Liu, L. Zheng, F. P. García de Arquer, C. T. Dinh, F. Fan, M. Yuan, E. Yassitepe, N. Chen, T. Regier, P. Liu, Y. Li, P. De Luna, A. Janmohamed, H. L. Xin, H. Yang, A. Vojvodic and E. H. Sargent, *Science*, 2016, **352**, 333–337.
38 P. Du, J. Zhang, Y. Liu and M. Huang, *Electrochem. Commun.*, 2017, **83**, 11–15.
39 N. F. Rosli, C. C. Mayorga-Martinez, N. M. Latiff, N. Rohaizad, Z. Sofer, A. C. Fisher and M. Pumera, *ACS Sustainable Chem. Eng.*, 2018, **6**, 7432–7441.
40 X. J. Chua and M. Pumera, *Phys. Chem. Chem. Phys.*, 2017, **19**, 6610–6619.
41 C. Song and J. Zhang, in *PEM Fuel Cell Electrocatalysts and Catalyst Layers: Fundamentals and Applications*, ed. J. Zhang, Springer London, London, 2008, pp. 89–134, DOI: 10.1007/978-1-84800-936-3_2.
42 Y. Jiao, Y. Zheng, M. Jaroniec and S. Z. Qiao, *Chem. Soc. Rev.*, 2015, **44**, 2060–2086.
43 E. S. Davydova, S. Mukerjee, F. Jaouen and D. R. Dekel, *ACS Catal.*, 2018, **8**(7), 6665–6690.

44 C. Domínguez, K. M. Metz, M. K. Hoque, M. P. Browne, L. Esteban-Tejeda, C. K. Livingston, S. Lian, T. S. Perova and P. E. Colavita, *ChemElectroChem*, 2018, **5**, 62–70.
45 J. S. Kim, B. Kim, H. Kim and K. Kang, *Adv. Energy Mater.*, 2018, **8**(11), 1702774.
46 J.-X. Feng, H. Xu, Y.-T. Dong, S.-H. Ye, Y.-X. Tong and G.-R. Li, *Angew. Chem., Int. Ed.*, 2016, **55**, 3694–3698.
47 J.-X. Feng, S.-H. Ye, H. Xu, Y.-X. Tong and G.-R. Li, *Adv. Mater.*, 2016, **28**, 4698–4703.
48 X.-F. Lu, L.-F. Gu, J.-W. Wang, J.-X. Wu, P.-Q. Liao and G.-R. Li, *Adv. Mater.*, 2017, **29**, 1604437.
49 S.-H. Ye, Z.-X. Shi, J.-X. Feng, Y.-X. Tong and G.-R. Li, *Angew. Chem., Int. Ed.*, 2018, **57**, 2672–2676.
50 M. Xing, L.-B. Kong, M.-C. Liu, L.-Y. Liu, L. Kang and Y.-C. Luo, *J. Mater. Chem. A*, 2014, **2**, 18435–18443.
51 R. D. L. Smith, M. S. Prévot, R. D. Fagan, S. Trudel and C. P. Berlinguette, *J. Am. Chem. Soc.*, 2013, **135**, 11580–11586.
52 L. Trotochaud, J. K. Ranney, K. N. Williams and S. W. Boettcher, *J. Am. Chem. Soc.*, 2012, **134**, 17253–17261.
53 C. Bocca, A. Barbucci, M. Delucchi and G. Cerisola, *Int. J. Hydrogen Energy*, 1999, **24**, 21–26.
54 M. Gao, W. Sheng, Z. Zhuang, Q. Fang, S. Gu, J. Jiang and Y. Yan, *J. Am. Chem. Soc.*, 2014, **136**, 7077–7084.
55 S. Klaus, M. W. Louie, L. Trotochaud and A. T. Bell, *J. Phys. Chem. C*, 2015, **119**, 18303–18316.
56 J. R. Swierk, S. Klaus, L. Trotochaud, A. T. Bell and T. D. Tilley, *J. Phys. Chem. C*, 2015, **119**, 19022–19029.
57 T. Takashima, K. Hashimoto and R. Nakamura, *J. Am. Chem. Soc.*, 2012, **134**, 1519–1527.
58 T. T. H. Hoang and A. A. Gewirth, *ACS Catal.*, 2016, **6**, 1159–1164.
59 M. K. Bates, Q. Jia, H. Doan, W. Liang and S. Mukerjee, *ACS Catal.*, 2016, **6**, 155–161.
60 M. Browne, R. J. Cullen, R. L. Doyle, P. E. Colavita and M. E. G. Lyons, *ECS Trans.*, 2013, **53**, 59–77.
61 M. P. Browne, H. Nolan, G. S. Duesberg, P. E. Colavita and M. E. G. Lyons, *ACS Catal.*, 2016, **6**, 2408–2415.
62 V. Nicolosi, M. Chhowalla, M. G. Kanatzidis, M. S. Strano and J. N. Coleman, *Science*, 2013, **340**, 1226419.
63 K. Kalantar-zadeh, J. Z. Ou, T. Daeneke, A. Mitchell, T. Sasaki and M. S. Fuhrer, *Appl. Mater. Today*, 2016, **5**, 73.
64 M. Zeng, Y. Xiao, J. Liu, K. Yang and L. Fu, *Chem. Rev.*, 2018, **118**(13), 6236–6296.
65 S. Yang, Y. Gong, Z. Liu, L. Zhan, D. P. Hashim, L. Ma, R. Vajtai and P. M. Ajayan, *Nano Lett.*, 2013, **13**, 1596–1601.
66 F. Song and X. Hu, *J. Am. Chem. Soc.*, 2014, **136**, 16481–16484.
67 F. Song and X. Hu, *Nat. Commun.*, 2014, **5**, 4477.
68 Q. Wang and D. O'Hare, *Chem. Rev.*, 2012, **112**, 4124–4155.
69 R. Ma, Z. Liu, K. Takada, N. Iyi, Y. Bando and T. Sasaki, *J. Am. Chem. Soc.*, 2007, **129**, 5257–5263.
70 J. Coelho, B. Mendoza-Sánchez, H. Pettersson, A. Pokle, E. K. McGuire, E. Long, L. McKeon, A. P. Bell and V. Nicolosi, *2D Mater.*, 2015, **2**, 2.
71 L. Zhu, C. K. Nuo Peh, T. Zhu, Y.-F. Lim and G. W. Ho, *J. Mater. Chem. A*, 2017, **5**, 8343–8351.
72 H. Jiang, H. Ma, Y. Jin, L. Wang, F. Gao and Q. Lu, *Sci. Rep.*, 2016, **6**, 31751.
73 Y. Zhu, C. Cao, S. Tao, W. Chu, Z. Wu and Y. Li, *Sci. Rep.*, 2014, **4**, 5787.
74 Z. Tianran, G. Xiaoming, Z. Zhao, T. N. Neng, L. Zhaolin, F. Adrian and L. J. Yang, *ChemCatChem*, 2018, **10**, 422–429.
75 S. Jaśkaniec, C. Hobbs, A. Seral-Ascaso, J. Coelho, M. P. Browne, D. Tyndall, T. Sasaki and V. Nicolosi, *Sci. Rep.*, 2018, **8**, 4179.
76 D. McAteer, I. J. Godwin, Z. Ling, A. Harvey, L. He, C. S. Boland, V. Vega-Mayoral, B. Szydłowska, A. A. Rovetta, C. Backes, J. B. Boland, X. Chen, M. E. G. Lyons and J. N. Coleman, *Adv. Energy Mater.*, 2018, **8**(15), 1702965.
77 M. H. Alfaruqi, S. Islam, D. Y. Putro, V. Mathew, S. Kim, J. Jo, S. Kim, Y.-K. Sun, K. Kim and J. Kim, *Electrochim. Acta*, 2018, **276**, 1–11.
78 A. Harvey, X. He, I. J. Godwin, C. Backes, D. McAteer, N. C. Berner, N. McEvoy, A. Ferguson, A. Shmeliov, M. E. G. Lyons, V. Nicolosi, G. S. Duesberg, J. F. Donegan and J. N. Coleman, *J. Mater. Chem. A*, 2016, **4**, 11046–11059.
79 A. A. S. Rovetta, M. P. Browne, A. Harvey, I. J. Godwin, J. N. Coleman and M. E. G. Lyons, *Nanotechnology*, 2017, **28**, 375401.
80 Y. Jia, L. Zhang, G. Gao, H. Chen, B. Wang, J. Zhou, M. T. Soo, M. Hong, X. Yan, G. Qian, J. Zou, A. Du and X. Yao, *Adv. Mater.*, 2017, **29**, 1700017.
81 V. V. Atuchin, T. A. Gavrilova, T. I. Grigorieva, N. V. Kuratieva, K. A. Okotrub, N. V. Pervukhina and N. V. Surovtsev, *J. Cryst. Grow.*, 2011, **318**, 987–990.
82 G. P. Wirtz, L. B. Sis and J. S. Wheeler, *J. Catal.*, 1975, **38**, 196–205.
83 H. Tao, Y. Zhang, Y. Gao, Z. Sun, C. Yan and J. Texter, *Phys. Chem. Chem. Phys.*, 2017, **19**, 921–960.
84 S. Chandrasekaran, E. J. Kim, J. S. Chung, C. R. Bowen, B. Rajagopalan, V. Adamaki, R. D. K. Misra and S. H. Hur, *J. Mater. Chem. A*, 2016, **4**, 13271–13279.
85 F.-C. Shen, Y. Wang, Y.-J. Tang, S.-L. Li, Y.-R. Wang, L.-Z. Dong, Y.-F. Li, Y. Xu and Y.-Q. Lan, *ACS Energy Lett.*, 2017, **2**, 1327–1333.
86 T. Kidd, A. O'Shea, K. Boyle, J. Wallace and L. Strauss, *Nanoscale Res. Lett.*, 2011, **6**, 294.
87 C. Zhao, H. Zhang, W. Si and H. Wu, *Nat. Commun.*, 2016, **7**, 12543.
88 H. Kim, J. Hong, K.-Y. Park, H. Kim, S.-W. Kim and K. Kang, *Chem. Rev.*, 2014, **114**, 11788–11827.
89 F. Wang, S. Xiao, Y. Hou, C. Hu, L. Liu and Y. Wu, *RSC Adv.*, 2013, **3**, 13059–13084.
90 S. Miyazaki, S. Kikkawa and M. Koizumi, *Synth. Met.*, 1983, **6**, 211–217.
91 D. Montasserasadi, D. Mohanty, A. Huq, L. Heroux, E. A. Payzant and J. B. Wiley, *Inorg. Chem.*, 2014, **53**, 1773–1778.
92 H. T. Lee, S. Kwon, C. M. Youn, T. Choi and J. H. Lee, *Eur. J. Inorg. Chem.*, 2017, 2184–2189.
93 J. Luxa, P. Vosecký, V. Mazánek, D. Sedmidubský, M. Pumera and Z. Sofer, *ACS Catal.*, 2018, **8**, 2774–2781.
94 M. P. Browne and A. Mills, *J. Mater. Chem. A*, 2018, **6**, 14162–14169.

95 A. Corina, B. Stefan, V. Edgar, M. Justus, V. Eugeniu, K. Bharathi, M. Sandra and S. Wolfgang, *Angew. Chem., Int. Ed.*, 2017, **56**, 11258–11262.
96 I. J. Godwin and M. E. G. Lyons, *Electrochem. Commun.*, 2013, **32**, 39–42.
97 R. L. Doyle, I. J. Godwin, M. P. Brandon and M. E. G. Lyons, *Phys. Chem. Chem. Phys.*, 2013, **15**, 13737–13783.
98 S. R. Mellsop, A. Gardiner, B. Johannessen and A. T. Marshall, *Electrochim. Acta*, 2015, **168**, 356–364.
99 S. Klaus, Y. Cai, M. W. Louie, L. Trotochaud and A. T. Bell, *J. Phys. Chem. C*, 2015, **119**, 7243–7254.
100 M. P. Browne, S. Stafford, M. O'Brien, H. Nolan, N. C. Berner, G. S. Duesberg, P. E. Colavita and M. E. G. Lyons, *J. Mater. Chem. A*, 2016, **4**, 11397–11407.
101 D. A. Corrigan, *J. Electrochem. Soc.*, 1987, **134**, 377–384.
102 L. Trotochaud, S. L. Young, J. K. Ranney and S. W. Boettcher, *J. Am. Chem. Soc.*, 2014, **136**, 6744–6753.
103 X. Lu, W.-L. Yim, B. H. R. Suryanto and C. Zhao, *J. Am. Chem. Soc.*, 2015, **137**, 2901–2907.
104 Z. Yunxuan, C. Chao, T. Fei, Z. Yufei, C. Guangbo, S. Run, G. I. N. Waterhouse, H. Weifeng and Z. Tierui, *Adv. Energy Mater.*, 2017, **7**, 1700005.
105 M. Huynh, C. Shi, S. J. L. Billinge and D. G. Nocera, *J. Am. Chem. Soc.*, 2015, **137**, 14887–14904.
106 R. Frydendal, L. C. Seitz, D. Sokaras, T. C. Weng, D. Nordlund, I. Chorkendorff, I. E. L. Stephens and T. F. Jaramillo, *Electrochim. Acta*, 2017, **230**, 22–28.
107 Y. Meng, W. Song, H. Huang, Z. Ren, S.-Y. Chen and S. L. Suib, *J. Am. Chem. Soc.*, 2014, **136**, 11452–11464.
108 W. Hui, Z. Jiajia, H. Xudong, Z. Xiaodong, X. Junfeng, P. Bicai and X. Yi, *Angew. Chem., Int. Ed.*, 2015, **54**, 1195–1199.
109 H.-Y. Su, Y. Gorlin, I. C. Man, F. Calle-Vallejo, J. K. Norskov, T. F. Jaramillo and J. Rossmeisl, *Phys. Chem. Chem. Phys.*, 2012, **14**, 14010–14022.
110 A. C. Thenuwara, E. B. Cerkez, S. L. Shumlas, N. H. Attanayake, I. G. McKendry, L. Frazer, E. Borguet, Q. Kang, R. C. Remsing, M. L. Klein, M. J. Zdilla and D. R. Strongin, *Angew. Chem., Int. Ed.*, 2016, **55**, 10381–10385.
111 L. Su, H. Du, C. Tang, K. Nan, J. Wu and C. Ming Li, *J. Colloid Interface Sci.*, 2018, **528**, 36–44.
112 Z. Zhang, T. Zhang and J. Y. Lee, *ACS Appl. Nano Mater.*, 2018, **1**, 751–758.
113 N. Han, F. Zhao and Y. Li, *J. Mater. Chem. A*, 2015, **3**, 16348–16353.
114 M. Luo, Z. Cai, C. Wang, Y. Bi, L. Qian, Y. Hao, L. Li, Y. Kuang, Y. Li, X. Lei, Z. Huo, W. Liu, H. Wang, X. Sun and X. Duan, *Nano Res.*, 2017, **10**, 1732–1739.
115 X. Lu and C. Zhao, *Nat. Commun.*, 2015, **6**, 6616.
116 Y. Vlamidis, E. Scavetta, M. Gazzano and D. Tonelli, *Electrochim. Acta*, 2016, **188**, 653–660.
117 Y. Fengkai, S. Kirill, S. Ilya, A. Hendrik, B. Alexander, O. Kevin, X. Wei, M. Justus, G. Wolfgang, C. B. Roldan, S. Wolfgang and M. Martin, *ChemSusChem*, 2017, **10**, 156–165.
118 M. S. Burke, M. G. Kast, L. Trotochaud, A. M. Smith and S. W. Boettcher, *J. Am. Chem. Soc.*, 2015, **137**, 3638–3648.
119 A. M. Ullman, C. N. Brodsky, N. Li, S.-L. Zheng and D. G. Nocera, *J. Am. Chem. Soc.*, 2016, **138**, 4229–4236.
120 T. Zhan, Y. Zhang, X. Liu, S. Lu and W. Hou, *J. Power Sources*, 2016, **333**, 53–60.
121 L. Wang, C. K. Chua, B. Khezri, R. D. Webster and M. Pumera, *Electrochem. Commun.*, 2016, **62**, 17–20.
122 S. Jiri, L. Jan, P. Martin and S. Zdeněk, *Chem. – Eur. J.*, 2018, **24**, 5992–6006.
123 W. Wang, Y. Liu, J. Li, J. Luo, L. Fu and S. Chen, *J. Mater. Chem. A*, 2018, **6**, 14299–14306.
124 M. Oliver-Tolentino, J. Vazquez-Samperio, M. Tufiño-Velázquez, J. Flores-Moreno, L. Lartundo-Rojas and R. de G. Gonzalez-Huerta, *J. Appl. Electrochem.*, 2018, **48**, 947–957.
125 X. Jia, S. Gao, T. Liu, D. Li, P. Tang and Y. Feng, *Electrochim. Acta*, 2017, **245**, 59–68.